Transverse laser patterns. I. Phase singularity crystals

M. Brambilla* and F. Battipede
Dipartimento di Fisica, Università di Milano, Italy

L. A. Lugiato, V. Penna, and F. Prati*
Dipartimento di Fisica, Politecnico di Torino, corso Duca degli Abruzzi 24, 10129 Torino, Italy

C. Tamm
Physicalisch-Technische Bundesanstalt, Braunschweig, Germany

C. O. Weiss
Department of Physics, University of Queensland, St. Lucia, Australia
(Received 12 July 1990)

We analyze the interaction and the competition of a set of transverse cavity modes, which belong to a frequency-degenerate family. The laser turns out to be able to realize several different stationary spatial patterns, which differ in the transverse configuration of the intensity or of the field and are met by varying the values of the control parameters. A striking feature that emerges in almost all steady-state patterns is the presence of dark points, in which both the real and the imaginary part of the electric field vanish and such that, if one covers a closed loop around one of these points, the field phase changes by a multiple of 2π, which corresponds to the topological charge of the point. We show in detail the analogy of these *phase singularities* to the vortex structures well known in such fields as, for example, hydrodynamics, superconductivity, and superfluidity. In our case, at steady state, these singularities are arranged in the form of regular *crystals*, and the equiphase lines of the field exhibit a notable similarity to the field lines of the electrostatic field generated by a corresponding set of point charges. We analyze in detail the patterns that emerge in the cases $2p+l=2$ and $2p+l=3$, where p and l are the radial and angular modal indices, respectively, and we compare the results with the experimental observations obtained from a Na_2 laser. The observed patterns agree in detail with those found by theory; in particular, they exhibit the predicted phase singularities in each pattern. The transitions from one pattern to another, that one observes under variation of the control parameters, basically agree with those predicted by theory.

I. INTRODUCTION

The analysis of temporal, spatial, and spatiotemporal phenomena is the central theme in the broad field of nonlinear dynamical systems. In the case of nonlinear optics, the last 15 years witnessed very extensive investigations of the temporal effects such as, for example, the onset of spontaneous oscillations in the output intensity emitted by a cavity filled with a nonlinear material, quasiperiodic or chaotic behavior.[1–4] One of the major results in this framework was the experimental observation of Lorenz-like chaos in far-infrared (FIR) lasers.[5] The dominant interest in the time aspects was due mainly to the use of the plane-wave approximation, which assumes the uniformity of the electric field in the planes orthogonal to the direction of propagation of the radiation beam. This approximation drastically simplifies the mathematical complexity of the models used to describe nonlinear optical systems, but, on the other hand, it eliminates all the spatial effects that may arise in the transverse directions. It is most interesting, therefore, to eliminate the rigidity imposed by the plane-wave approximation, because one can expect to find in optics phenomena similar to those which are familiar in other fields such as, for example, nonlinear chemical reactions, hydrodynamics, and biology.[6–8] In these fields the spatial effects are due and are controlled by diffusion, whereas in optics the role of diffusion is played by diffraction.

Apart from a number of pioneering works in the 1960s,[9–11] the systematic investigation of transverse effects started in relatively recent times. It was initially devoted to passive systems[12–16] and only later focused also on laser systems.[17–24] Two special issues on transverse phenomena in nonlinear optical systems will appear soon in the Journal of the Optical Society of America.[25]

The onset of spatial and spatiotemporal phenomena in laser is governed by the interaction and competition among the modes of the empty cavity, which is in turn controlled by the spatial configuration of each mode with respect to that of the available gain and of the loss profile, and by the different frequency of each mode. In general, we can distinguish three regimes of operation in the laser.

(i) The single-mode regime, in which one transverse mode dominates over the others and imposes its frequency and its spatial configuration.

(ii) The standard multimode regime, in which at least

two transverse modes give a significant contribution to the output field and, because of their different frequencies, interfere with one another, giving rise to an output intensity which oscillates in time, also with respect to the transverse configuration. According to the number of competing modes, the oscillations may be periodic, quasiperiodic, or chaotic. From a spatiotemporal viewpoint, the behavior can vary from simple to apparently very complex. The issue of complexity, and the possible relations with spatio-temporal turbulence, are presently a matter of investigation.[24]

(iii) The cooperatively frequency-locked multimode regime,[19,21,24] in which at least two transverse modes contribute significantly to the output field, and lock to a common frequency with which they oscillate in a synchronized way. The locking concerns also the relative phases of the modes, so that the output intensity has a stationary transverse configuration, exactly as in the case of the single-mode regime. The common oscillation frequency, cooperatively selected by the modes, corresponds to the average of the modal frequencies, weighted over the intensity distribution of the modes in the stationary state. The prediction of the phenomenon of cooperative frequency locking has received experimental confirmation recently.[26,27]

In this joint theoretical-experimental investigation we focus on the case of a ring laser with spherical mirrors and with cylindrical symmetry around the laser axis. We assume conditions such that the gain line can excite only a frequency-degenerate family of Gauss-Laguerre modes, i.e., the modes such that $2p+l=q$ with q fixed, where p and l are the radial and the angular index of the modes. In this condition there is no frequency competition among the modes, so that the phenomenon of cooperative locking is necessary for the formation of stationary states only in the sense of producing the phase locking.

We analyze in detail the cases $q=2$ and 3, in which the competition involves three or four modes of the empty cavity, respectively. We find that the laser is able to realize a number of different stationary spatial patterns that are met by changing the values of the control parameters such as, for example, the pump parameter or the width of the pumped region. It must be noted that these stationary configurations of the laser must not be confused with "modes of the active resonator." As a matter of fact, in the empty resonator, the Gauss-Laguerre modes can be linearly superimposed in all possible combinations, whereas in the filled cavity, each stationary state is an attractor in the phase space of the system, such that the system approaches one or the other of these attractors, without possibility of realizing any linear combination of them. The variation of the control parameters induces continuous and discontinuous transitions among the different transverse patterns which are found both in the numerical computations and in the experimental observations, with a very satisfactory qualitative agreement between theory and experiment. An example of such transitions is the process of spontaneous breaking of the cylindrical symmetry theoretically predicted in Ref. 23 and experimentally observed recently.[28]

In the process of transverse pattern selection of the laser field, the phase of the envelope of the electric field plays a crucial role. A striking feature in the laser patterns, which we calculated and observed experimentally, is the presence of isolated points in the transverse plane which are characterized by the following features.

(a) In correspondence to these points both the real and the imaginary parts of the electric field vanish, hence these points appear as dark spots in the laser-beam section.

(b) Around each of these points the modulus of the electric field raises from zero in the form of an inverted cone with a more or less steep gradient.

(c) If one performs a closed counterclockwise loop which surrounds one of these points, the phase of the envelope of the electric field changes by a quantity equal to $\pm 2\pi m$, where m is a positive integer.

The phase variation of $\pm 2\pi m$, which is the phase-gradient circuitation, implies that the electric-field phase is a multivalued function and the point in question is a singularity of the phase. In the literature, $\pm m$ is called "topological charge." This nomenclature arises from the striking similarity of the *phase-gradient* field lines (in the present case the phase is that of the electric field) with the field lines of the magnetic field generated by a set of straight wire currents. The circuitation around the wires on a reference transverse plane is the topological charge of the plane punctured by the wires. This type of exotic configurations of the field is well known in condensed-matter physics,[29] where the onset of configurations with defects in the medium leads to states of the system which are thermodynamically favorable. Defects are also called "topological excitations," since they describe a spatial complexity of topological type.[30] They configurate as vortices in superfluid media, spin vortices in magnetic spin systems, and dislocations in crystals,[31] and correspond to singularities of the phase of the order parameter which locally describes the physical state at each point of the medium. In the present context, the electric field plays the role of a complex-valued order parameter whose phase singularities are mathematically described, by the same analytical structure of two-dimensional pointlike vortices in hydrodynamics.[32]

The properties (a)–(c) are fulfilled also in the "optical vortices" recently discovered by Coullet and collaborators[33] in their two-dimensional analysis of the model formulated in Ref. 19. A major difference arises, on the other hand, from the fact that the vortices of Ref. 33 can be generated in any position of the transverse plane, whereas the singularities which appear in the stationary configurations of our laser system are located in precisely defined positions, even if they are able to move during the transient evolution towards the stationary configuration. In addition, in the case of the structures that we analyze, the *equiphase lines* of the laser field exhibit an impressive similarity with the field lines of the electric field generated by a set of point charges; this similarity is absent in the case of the optical vortices of Ref. 33. For these reasons we prefer to designate with the name "phase singularities" the dark points in our laser patterns, instead of using the nomenclature "optical vortices."

A dominant feature of our phase singularities is that

they are arranged in the form of regular geometric arrays, i.e., crystals which are reminescent of the ionic crystals recently realized in ionic traps.[34] For this reason we call these structures *phase singularity crystals.*

In Sec. II we introduce the dynamical equations which govern the competition among the modes of a frequency-degenerate family and calculate the stationary solutions corresponding to a single Gauss-Laguerre mode as well as the two-mode (also called doughnut) stationary solutions and discuss their stability; finally, we define the notion of phase singularity.

Section III is devoted to the description of the different patterns that arise in the case of the simplest frequency-degenerate families, namely $q=1$, 2, and 3. We specify the region in the parameter space where each pattern appears, and the continuous and discontinuous transitions from one pattern to another that one finds when the control parameters are varied.

In Sec. IV we illustrate in detail the analogy between the phase singularities that we find in the transverse configuration of the electric field and the well-known vortex structures in fluids; on the basis of the concept of order parameter, this analogy is extended to other fields as superconductors, superfluids, and so on.

Section V is devoted to the experimental results; we describe the laboratory setting, illustrate the experimental observations, and compare them with the theoretical predictions. Some concluding remarks are given in Sec. VI.

II. MODE-MODE COMPETITION OF A FREQUENCY-DEGENERATE FAMILY OF MODES

We consider a ring laser with spherical mirrors and assume that the length of the active region is much smaller than the Rayleigh length of the cavity. This circumstance allows us to neglect the longitudinal variations of the beam width and field phase along the active sample. Actually this restriction is not essential for the nature of the results that we will derive and can be easily dropped; however, we prefer to use it in order to keep our calculations as simple as possible. Hence, for a cylindrically symmetrical cavity, the transverse profile of the cavity modes is described by the functions[35]

$$A_{p0}(\rho,\varphi)=\frac{2}{\sqrt{2\pi}}L_p^0(2\rho^2)e^{-\rho^2},$$
$$A_{pli}(\rho,\varphi)=\frac{2}{\sqrt{\pi}}(2\rho^2)^{l/2}\left[\frac{p!}{(p+l)!}\right]^{1/2}\times L_p^l(2\rho^2)e^{-\rho^2}\times\begin{cases}\cos(l\varphi), & i=1\\ \sin(l\varphi), & i=2\end{cases}, \quad (2.1)$$

where $p=0,1,\ldots$ is the radial index and $l=0,1,\ldots$ is the angular index, ρ denotes the radial coordinate $r=(x^2+y^2)^{1/2}$ normalized to the beam waist w, and L_p^l are Laguerre polynomials of the indicated argument. The functions A_{pli} obey the orthonormality relation

$$\int_0^{2\pi}d\varphi\int_0^{\infty}d\rho\,\rho\,A_{pli}(\rho,\varphi)A_{p'l'i'}(\rho,\varphi)=\delta_{pp'}\delta_{ll'}\delta_{ii'}. \quad (2.2)$$

We assume that the active medium is a homogeneously broadened system of two-level atoms with transition frequency ω_a and linewidth $\gamma_\perp$, and that the excited region has a Gaussian transverse shape of radius r_p; i.e., the transverse configuration of the equilibrium population inversion is described by the function

$$\chi(\rho)=\exp(-2\rho^2/\psi^2),\quad \psi=2r_p/w. \quad (2.3)$$

We observe that our choice of the Gauss-Laguerre modes (2.1) as the basis is in part arbitrary; we might use, alternatively, the Gauss-Hermite modes TEM_{nm}, or the Gauss doughnut modes B_{pli} introduced in Sec. II C. The fact that the pump profile is cylindrically symmetrical makes it more convenient to use the Gauss-Laguerre or Gauss doughnut modes, because a subset of the modes (precisely those with $l=0$) are cylindrically symmetric.

A. Nonlinear dynamical equations and steady-state equations

An important property of the Gauss-Laguerre modes is that their frequency depends on the transversal mode indices p and l via the combination $2p+l$, a situation that produces mode degeneracy. We assume now that the atomic line is near resonance with a frequency-degenerate family of transverse modes corresponding to a given value of the longitudinal modal index, and such that $2p+l=q$, with q fixed. We call ω_q the common frequency of the modes of the family. We suppose, in addition, that all the other cavity modes either suffer from large losses, or their frequency separation from the atomic line is much larger than the atomic linewidth; therefore only the modes belonging to the frequency-degenerate family take part in the laser emission. Hence the laser field has the form

$$E(\rho,\varphi,z,t)\propto F(\rho,\varphi,z,t)\exp(-i\bar{\omega}_q t+ik_q z)+\text{c.c.}, \quad (2.4)$$

where F is the normalized slowly varying envelope, $k_q=\omega_q/c$ is the common wave number of the modes of the family, and $\bar{\omega}_q$ is the mode-pulled frequency

$$\bar{\omega}_q=\frac{\omega_a k+\omega_q\gamma_\perp}{k+\gamma_\perp}; \quad (2.5)$$

k is the cavity damping constant

$$k=\frac{cT}{\mathcal{L}}, \quad (2.6)$$

where T is the transmissivity coefficient of the mirrors and $\mathcal{L}$ is the total length of the ring cavity. In turn, the envelope F can be expanded as follows:

$$F(\rho,\varphi,t)=\sum_{p,l,i}{}'f_{pli}(t)A_{pli}(\rho,\varphi), \quad (2.7)$$

where the prime indicates that the sum is restricted to the modes of the family. The modal amplitudes f_{pli} obey the time-evolution equations[23]

$$\frac{df_{pli}}{dt}=-k\left[(1-i\Delta)f_{pli}-2C\int_0^{2\pi}d\varphi\int_0^{\infty}d\rho\,\rho\,A_{pli}(\rho,\varphi)P(\rho,\varphi,t)\right]; \quad (2.8)$$

Δ is the detuning parameter

$$\Delta=\frac{\bar{\omega}_q-\omega_q}{k}=\frac{\omega_a-\bar{\omega}_q}{\gamma_\perp} , \tag{2.9}$$

C is the pump parameter

$$C=\frac{\alpha L}{2T} , \tag{2.10}$$

where α is the gain parameter per unit length of the field and L is the length of the active region; P is the normalized slowly varying envelope of the atomic polarization. Equation (2.8) must be coupled with the atomic Bloch equations, which read

$$\frac{\partial P}{\partial t}=\gamma_\perp[F(\rho,\varphi,t)D(\rho,\varphi,t)-(1+i\Delta)P(\rho,\varphi,t)] , \tag{2.8'}$$

$$\frac{\partial D}{\partial t}=-\gamma_\parallel\{\mathrm{Re}[F^*(\rho,\varphi,t)P(\rho,\varphi,t)]+D(\rho,\varphi,t)-\chi(\rho)\} , \tag{2.8''}$$

where D is the normalized population inversion and $\gamma_\parallel$ is its relaxation rate. In Eqs. (2.8') and (2.8'') it is understood that F is given by the expansion (2.7); thus Eqs. (2.8) form a self-contained set of equations for the variables f_{pli}, P and D.[36] In the steady state one obtains from Eqs. (2.8') and (2.8'')

$$D=\frac{1+\Delta^2}{1+\Delta^2+|F(\rho,\varphi)|^2}\chi(\rho) ,$$
$$P=\frac{(1-i\Delta)F(\rho,\varphi)}{1+\Delta^2+|F(\rho,\varphi)|^2}\chi(\rho) , \tag{2.11}$$

so that Eqs. (2.8) become

$$f_{pli}=2C\sum_{p',l',i'}{}'\int_0^{2\pi}d\varphi\int_0^{\infty}d\rho\,\rho\frac{A_{pli}(\rho,\varphi)A_{p'l'i'}(\rho,\varphi)}{1+\Delta^2+|F(\rho,\varphi)|^2}\chi(\rho)f_{p'l'i'} . \tag{2.12}$$

Of course, Eqs. (2.12) admit the trivial stationary solution $f_{pli}=0$ for all the choices of the indices p, l, and i in the family.

B. Single-mode stationary solutions

The set of stationary equations (2.12) admits also exact single-mode solutions, in each of which only one transverse mode is excited, while the amplitudes of all the other modes are exactly equal to zero. Thus the solution in which the mode (pli) is excited obeys the steady-state equation

$$1=2C\int_0^{2\pi}d\varphi\int_0^{\infty}d\rho\,\rho\frac{A_{pli}^2(\rho,\varphi)\chi(\rho)}{1+\Delta^2+A_{pli}^2(\rho,\varphi)|f_{pli}|^2} , \tag{2.13}$$

which determines the behavior of $|f_{pli}|^2$ as a function of the pump parameter C, while the phase or f_{pli} remains aribitrary. The threshold for this solution, which corresponds to the case $f_{pli}=0$, is given by

$$2C_{\mathrm{thr}}^{(pli)}=(1+\Delta^2)\times\left[\int_0^{2\pi}d\varphi\int_0^{\infty}d\rho\,\rho A_{pli}^2(\rho,\varphi)\chi(\rho)\right]^{-1} . \tag{2.14}$$

In the limit of a flat pump profile [i.e., for $\psi\to\infty$, which implies $\chi(\rho)=1$], using Eq. (2.2) we obtain immediately that all single-mode stationary solutions have the same threshold $2C_{\mathrm{thr}}=(1+\Delta^2)$. On the other hand, the situation of ψ finite favors the modes of the family which lies nearest to the laser axis. For example, when q is even, the family contains one cylindrically symmetrical mode with $l=0$, which has the lowest threshold.

The cylindrically symmetrical solutions ($p0$) are stable beyond threshold for an interval of C values which depends on p and tends to zero as ψ tends to infinity. On the other hand, all the asymmetrical single-mode stationary solutions are unstable. As a matter of fact, the mechanism which determines the stability is spatial hole-burning and cross-saturation. The single-mode stationary solution (pli) becomes unstable when another mode of the family $(\bar{p}\,\bar{l}\,\bar{i})\neq(pli)$ experiences a residual gain which exceeds the losses; precisely, the instability condition is

$$2C\int_0^{2\pi}d\varphi\int_0^{\infty}d\rho\,\rho\frac{A_{\bar{p}\,\bar{l}\,\bar{i}}^2(\rho,\varphi)\chi(\rho)}{1+\Delta^2+A_{pli}^2(\rho,\varphi)|f_{pli}|^2}>1 \tag{2.15}$$

for at least one choice of $(\bar{p}\,\bar{l}\,\bar{i})\neq(pli)$ belonging to the family. In the case of the single-mode stationary solution corresponding to the asymmetrical modes, the instability condition is already satisfied immediately above the threshold $C=C_{\mathrm{thr}}^{(pli)}$, given by Eq. (2.14), where $|f_{pli}|^2=0$. For example, the single-mode stationary solution corresponding to the sine mode is unstable against the growth of the cosine mode, and vice versa.

C. Two-mode stationary solutions

An especially simple class of multimode stationary solutions is formed by the states which arise from the combination of the two modes A_{pli}, $i=1,2$, for $l\neq0$, with equal amplitudes $|f_{pli}|$ and a phase difference of $+\pi/2$ or $-\pi/2$. These two structures have the form

$$B_{pli}(\rho,\varphi)=\left[\frac{2}{\pi}\right]^{1/2}(2\rho^2)^{l/2}\left[\frac{p!}{(p+l)!}\right]^{1/2}\times L_p^l(2\rho^2)e^{-\rho^2}e^{\pm il\varphi} , \tag{2.16}$$

where the index $i=1,2$ means that $i=1$ ($i=2$) corresponds to the $+$ ($-$) choice. Hence they have the same intensity configuration which corresponds to one or more rings around the origin; for this reason these structures are usually called doughnuts. On the other hand, the field configuration is different for the two states and is not cylindrically symmetrical. As a matter of fact, the two patterns (2.16) are obtained one from the other by per-

forming the parity transformation $\varphi \rightarrow -\varphi$ or the phase conjugation operation.

The doughnut stationary states have the form

$$F(\rho,\varphi)=B_{pli}(\rho,\varphi)g_{pli} \ ; \tag{2.17}$$

the modulus of g_{pli} is determined by a state equation identical to Eq. (2.13), upon substitution of A_{pli}^2 by $|B_{pli}|^2$ and f_{pli} by g_{pli}. In Eq. (2.13), in the doughnut case, the integration over φ can be replaced by a factor 2π, because the integrand is independent of φ. The same holds for the expression (2.14) of the threshold.

When $q=2p+l$ is odd, the doughnut state with $l=1$ has a domain of stability immediately above threshold and becomes unstable when the pump parameter C is increased enough, with the exception of the case $q=1$, where the solutions remain stable over all the parameter space. On the other hand, all the other stationary solutions of the doughnut type, for any value of q, are unstable immediately above threshold, but become stable when C is increased, over a suitable interval of C values. The functions B_{pli} obey the orthonormality relation

$$\int_0^{2\pi} d\varphi \int_0^{\infty} d\rho\, \rho B_{pli}^*(\rho,\varphi)B_{p'l'i'}(\rho,\varphi)=\delta_{pp'}\delta_{ll'}\delta_{ii'} \ . \tag{2.18}$$

D. Phase singularities

With the exception of the symmetrical single-mode stationary solutions, all other stable stationary solutions display isolated points in the transverse plane, where both the real and the imaginary parts of the electric-field envelope vanish simultaneously, so that these points appear as dark spots in the distribution of the output intensity. In addition, if one considers a closed counterclockwise loop l (Fig. 1) which surrounds one and only one of these points S, one has that the total variation of the phase of F over the loop is an integer multiple of 2π; precisely, if we set

$$F=|F|e^{i\Phi} \ , \tag{2.19}$$

we have

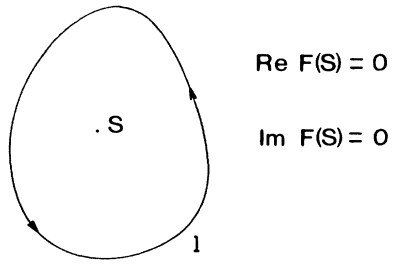

FIG. 1. In correspondence to point S both the real and the imaginary part of the electric field vanish. The total variation of the phase of F over the loop l is equal to an integer multiple of 2π.

$$\Delta\Phi=\int_l \nabla\Phi\cdot dl=\pm m\,2\pi \ , \tag{2.20}$$

where m is a positive integer. We call these structures "phase singularities," because they correspond to singularities of the vector field $\nabla\Phi$.

We also call the number $+m$ or $-m$ "charge" of the singularity; this is a topological charge, as explained in the Introduction and in Sec. IV. We will also see that there is a remarkable similarity between the equiphase lines of $F(\rho,\varphi)$ and the lines of force of a corresponding set of point electric charges.

It must be kept in mind that, if one considers the whole electric field E instead of the envelope F, the equiphase lines rotate around each phase singularity with an angular velocity equal to the mode-pulled frequency $\bar{\omega}_q$; this effect arises from the factor $\exp(-i\bar{\omega}_q t)$ in Eq. (2.4). Precisely, the lines rotate clockwise (counterclockwise) around positively (negatively) charged singularities.

These phase singularity structures are very similar to the "optical vortices" predicted in Ref. 33, which are related in the same way to the simultaneous vanishing of ReF and ImF, and to the property (2.20). On the other hand, a distinctive feature of the phase singularities that we find here, with respect to the optical vortices of Ref. 33, is the fact that they are arranged in the form of regular arrays, as we will see from several examples in the following. Hence we propose to call these structures *phase singularity crystals,* a name which emphasizes their similarity, for example, with ionic crystals in traps.[34] It is noteworthy that, even if the instability which leads to the onset of multimodal patterns arises from spatial holeburning, i.e., by a gain mechanism, the process of pattern formation is dominated by the phase, which gives rise to the singularities crystals.

III. DETAILED ANALYSIS OF SPECIFIC CASES

We shall now consider explicitly the behavior of our system in the cases $2p+l=1$ (two degenerate modes), $2p+l=2$ (three degenerate modes), and $2p+l=3$ (four degenerate modes), restricting our analysis to the tuned ($\Delta=0$) configuration, and solving the dynamical equations of our model. In all cases it is possible to use the basis of cavity modes A_{pli} [Eq. (2.1)] as well as the basis of the doughnut modes B_{pli} [Eq. (2.16)]. The main qualitative difference between these two possible choices is that the intensity profile of all modal functions is symmetrical in the latter case. It is equivalent to expand the electric field $F(\rho,\varphi,t)$ on either basis. In our description we choose the basis of the Gauss-doughnut modes B_{pli} because they can be stable steady states of the system, and in addition this choice allows one to discover simple relations between the amplitudes and the phases of the modal amplitudes when the laser operates in a multimode regime. Hence we write at steady state

$$F(\rho,\varphi)=\sum_{p,l,i}{}' g_{pli}B_{pli}(\rho,\varphi) \ , \tag{3.1}$$

where the sum is restricted to the modes of the degenerate family.

Despite the fact that the intensity patterns of both

$e^{+il\varphi}$ and $e^{-il\varphi}$ modes are identical, it turns out that it is possible to discriminate between them by means of the astigmatic observation technique described in Ref. 37. For each case we shall present a review of the stationary transverse patterns and of their stability, together with an analysis of the structure of the phase singularities and of the equiphase lines of the electric field.

A. The case $2p+l=1$

In this case the modes of the empty cavity are the two doughnut modes B_{011} and B_{012}, whose forms are

$$B_{011}=\left[\frac{2}{\pi}\right]^{1/2}(2\rho^2)^{1/2}e^{-\rho^2}e^{+i\varphi}\ , \tag{3.2a}$$

$$B_{012}=\left[\frac{2}{\pi}\right]^{1/2}(2\rho^2)^{1/2}e^{-\rho^2}e^{-i\varphi}\ . \tag{3.2b}$$

The intensity profile of these modes is shown in Fig. 2. From the general single-mode steady-state solution (2.13) we obtain the explicit equation

$$1=2C\int_0^\infty d\rho 4\rho\frac{2\rho^2e^{-2\rho^2}}{1+2\rho^2e^{-2\rho^2}x_i^2}\chi(\rho)\ , \tag{3.3}$$

where $x_i=\sqrt{2/\pi}|g_{01i}|$ $(i=1,2)$ are the scaled amplitudes for mode B_{01i} $(i=1,2)$.

The lasing threshold when the pump profile is given by (2.3) is derived from (2.14) and has the form

$$2C_{\rm thr}^{(01)}=\left[\frac{\psi^2+1}{\psi^2}\right]^2\ . \tag{3.4}$$

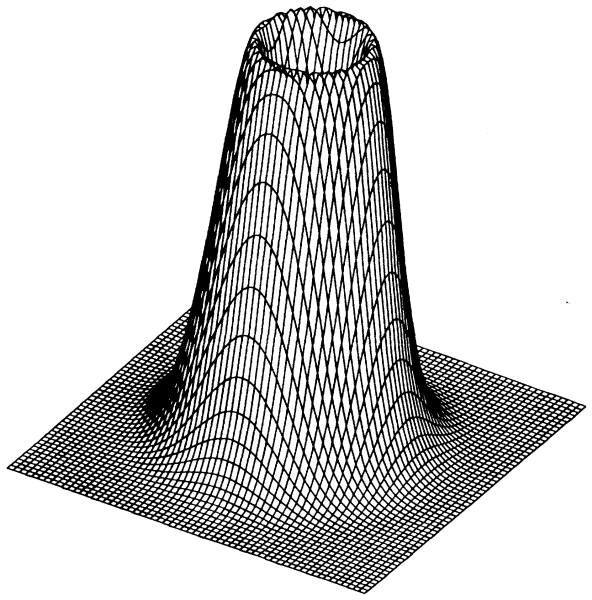

FIG. 2. Transverse intensity distribution in the doughnut pattern $2p+l=1$.

Figure 3 shows the steady-state curve for B_{01i} $(i=1,2)$ for some different values of ψ.

The stability condition for the B_{01i} $(i=1,2)$ steady states is given by

$$2CI\le 1\ , \tag{3.5}$$

where

$$I=\int_0^\infty d\rho 4\rho\frac{2\rho^2e^{-2\rho^2}}{(1+2\rho^2e^{-2\rho^2}x_i^2)^2}\chi(\rho)\ . \tag{3.6}$$

By using Eq. (3.3), one can rewrite Eq. (3.6) in the form

$$I=(2C)^{-1}-\int_0^\infty d\rho 4\rho\frac{(2\rho^2e^{-2\rho^2})^2x_i^2}{(1+2\rho^2e^{-2\rho^2}x_i^2)^2}\chi(\rho)\ , \tag{3.6'}$$

which immediately shows that condition (3.5) is satisfied for all values of the parameter C and ψ; that is, single-mode steady states B_{01i} $(i=1,2)$ are always stable. This implies that these two steady states coexist and there is bistability between them; this phenomenon was observed experimentally in Ref. 37.

These stationary solutions possess one phase singularity located at the origin. The equiphase lines are straight and depart radially from the origin, as shown in Fig. 4(a). Circuitation around the origin [see Eq. (2.20)] gives a phase accumulation of $+2\pi$ or -2π, i.e., a charge of ±1, depending on whether we are considering a B_{011} or a B_{012} solution.

B. The case $2p+l=2$

In this case the degenerate family consists of the three modes

$$A_{10}=\left[\frac{2}{\pi}\right]^{1/2}(1-2\rho^2)e^{-\rho^2}\ , \tag{3.7a}$$

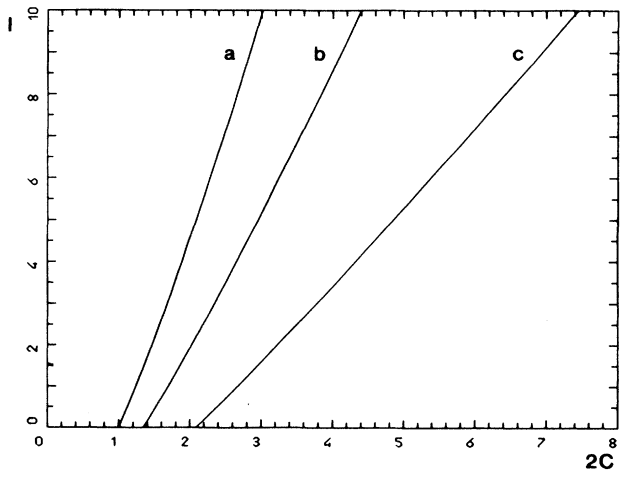

FIG. 3. Case $2p+l=1$. The total steady-state output intensity is graphed as a function of the pump parameter for the doughnut pattern and (a) $\psi\to\infty$, (b) $\psi=2.5$, (c) $\psi=1.5$.

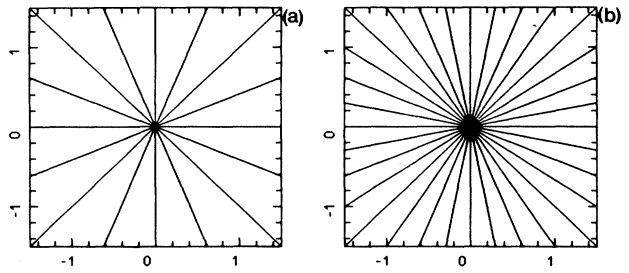

FIG. 4. Equiphase lines for the doughnut pattern (a) case $2p+l=1$, (b) case $2p+l=2$. The phase separation between adjacent lines is $\pi/8$ in both figures.

$$B_{021}=\left[\frac{1}{\pi}\right]^{1/2}2\rho^2e^{-\rho^2}e^{+2i\varphi}\ , \tag{3.7b}$$

$$B_{022}=\left[\frac{1}{\pi}\right]^{1/2}2\rho^2e^{-\rho^2}e^{-2i\varphi}\ . \tag{3.7c}$$

The single-mode steady-state equation for mode A_{10} reads explicitly

$$1=2C\int_0^\infty d\rho 4\rho\frac{(1-2\rho^2)^2e^{-2\rho^2}}{1+(1-2\rho^2)^2e^{-2\rho^2}x_1^2}\chi(\rho)\ , \tag{3.8}$$

while the doughnut solutions obey the stationary equation

$$1=2C\int_0^\infty d\rho 2\rho\frac{4\rho^4e^{-2\rho^2}}{1+2\rho^4e^{-2\rho^2}x_{2,3}^2}\chi(\rho)\ , \tag{3.9}$$

where x_i are the scaled amplitudes

$$x_1=\left[\frac{2}{\pi}\right]^{1/2}|g_{10}|\ , \tag{3.10a}$$

$$x_i=\left[\frac{2}{\pi}\right]^{1/2}|g_{02(i-1)}|,\quad i=2,3\ . \tag{3.10b}$$

The threshold for the A_{10} solution is

$$2C_{\rm thr}^{(10)}=\frac{(\psi^2+1)^3}{\psi^2(\psi^4+1)}\ , \tag{3.11}$$

while for the doughnut steady states it is

$$2C_{\rm thr}^{(02i)}=\frac{(\psi^2+1)^3}{\psi^6},\quad i=1,2\ . \tag{3.12}$$

It is evident that $2C_{\rm thr}^{(10)}\le 2C_{\rm thr}^{(02i)}$, where the equality holds in the limit of flat pump profile $\psi\to\infty$.

The analysis of the stability of the single-mode stationary states yields the following results: the A_{10} steady state is unstable for

$$\int_0^\infty d\rho 4\rho\frac{(-4\rho^4+8\rho^2-2)e^{-2\rho^2}}{1+(1-2\rho^2)^2e^{-2\rho^2}x_1^2}\chi(\rho)>0\ , \tag{3.13}$$

and the other two steady states are unstable for

$$\int_0^\infty d\rho 4\rho\frac{(4\rho^4-8\rho^2+2)e^{-2\rho^2}-8\rho^8e^{-4\rho^2}x_{2,3}^2}{(1+2\rho^4e^{-2\rho^2}x_{2,3}^2)^2}\chi(\rho)>0\ . \tag{3.14}$$

Figure 5 shows the regions of stability predicted by Eqs. (3.13) and (3.14) in the two-dimensional parameter space (C,ψ). Line 1 gives the lasing threshold for the A_{10} single-mode solution [Fig. 6(a)] according to Eqs. (3.11), while lines 2 and 4 give the instability thresholds governed by Eqs. (3.13) and (3.14), respectively. The lasing threshold for the doughnut solutions lies between lines 1 and 2, but we have not drawn it because these solutions are stable only on the right of line 4.

Summarizing, we can say that in region S (Fig. 5) only the symmetrical A_{10} single-mode steady-state solution is stable, in regions 4H and O-4H all the three stationary solutions with the configurations (3.7) are unstable, while in regions D-4H the A_{10} solution is unstable and the B_{02i} solutions are stable.

Therefore we expect that in regions 4H and O-4H and possibly in region D-4H some stable multimode stationary solution exists, given by a linear combination of the three modes of the basis:

$$F(\rho,\varphi)=A_{10}(\rho,\varphi)g_1+B_{021}(\rho,\varphi)g_2+B_{022}(\rho,\varphi)g_3\ . \tag{3.15}$$

We have systematically investigated the modal structure of the stable multimode stationary patterns in our system by solving the dynamical equations of the model. First of all, we must notice that in the expression (3.15) there is an overall arbitrary phase factor that we select,

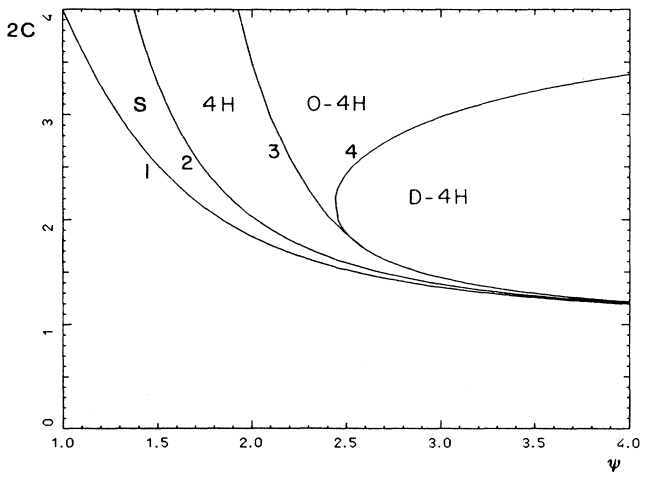

FIG. 5. Case $2p+l=2$. Phase-space diagram in the plane of the control parameters C,ψ. The abbreviations S, 4H, O, and D denote, respectively, symmetrical, four-hole, oval, and doughnut, and correspond to the patterns shown in Figs. 6(a), 6(b), 6(c), and 6(d), respectively. The letter in each region indicate the stable patterns.

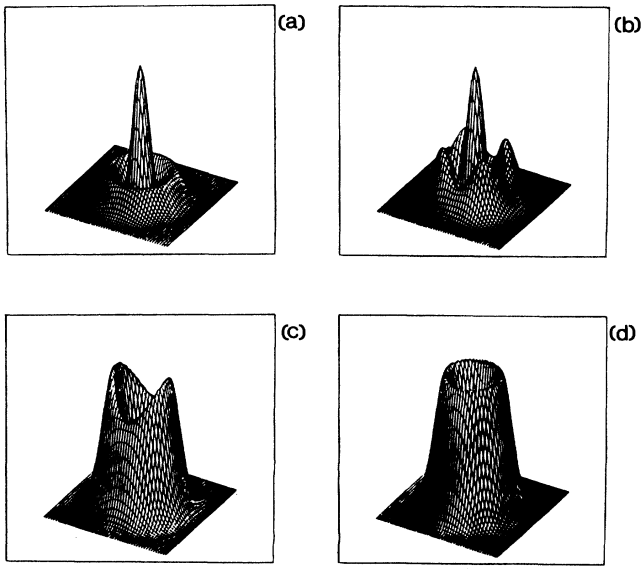

FIG. 6. Case $2p+l=2$. Transverse intensity distribution for the stable patterns. (a) Cylindrically symmetrical Gauss-Laguerre mode $p=1$, $l=0$; (b) the four-hole configuration; (c) the oval configuration; (d) doughnut.

for definiteness, in such a way that the amplitude g_1 is real and positive, so that Eq. (3.15) can be reformulated in the following way:

$$F(\rho,\varphi)=A_{10}(\rho,\varphi)g_1+B_{021}(\rho,\varphi)|g_2|e^{i\theta_2} +B_{022}(\rho,\varphi)|g_3|e^{i\theta_3} . \tag{3.16}$$

Each pattern generates an infinity of other possible patterns by rotation. From expansion (3.16) we note that if we perform a rotation of an angle φ_0, this is equivalent to changing the phases of the amplitudes of the doughnut modes from θ_2 to $\theta_2+2\varphi_0$ and from θ_3 to $\theta_3-2\varphi_0$. This implies that under rotation θ_2 and θ_3 can be varied arbitrarily, but their sum $\theta_2+\theta_3$ remains fixed. Hence the structure of each stationary multimode pattern depends only on the four quantities g_1, $|g_2|$, $|g_3|$, and $\theta_2+\theta_3$, while the orientation of the pattern in the transverse plane is determined by the particular values of θ_2 and θ_3. In all the multimode stationary solutions that we calculated, we found that $\theta_2+\theta_3=\pi$.

The multimode stationary configurations emerge in a continuous way when one leaves the domains of stability, that is, region S for the A_{10} solution and region D-4H for the doughnut solutions. For example, if one starts from a pure mode A_{10} in region S and passes through line 2 of Fig. 5, the system reaches a new stationary state where mode A_{10} is still dominant, but the two doughnut modes are present, too, with equal weight. The modal structure of this configuration is therefore characterized by the relation

$$|g_2|=|g_3| , \tag{3.17}$$

and its intensity profile is shown in Fig. 6(b). We call this the *four-hole* (4H) pattern since it has four black spots in its intensity profile. The domain of existence of the 4H mode is the whole region above line 2 of Fig. 5. The transition from the single-mode state A_{10} to the 4H-mode state, which arises at line 2 in Fig. 5, corresponds to the phenomenon of cylindrical symmetry breaking analyzed in Refs. 23 and 28. Simultaneously, also the parity symmetry $\varphi\rightarrow-\varphi$ is broken.

On the other hand, taking as an initial condition a pure doughnut solution in region D-4H and moving out from this region, a new pattern arises that has still a close resemblance to a doughnut, but with some distortion due to the small contributions of the other two modes. If the initial state of the system was, for definiteness, a pure mode B_{021}, the modal composition of the new configuration is such that

$$|g_2|\gg g_1\gg|g_3| . \tag{3.18}$$

The intensity profile of this pattern is shown in Fig. 6(c), and because of its overall shape we shall refer to it as *oval*. The oval exists in the O-4H region. From the viewpoint of the intensity the transition from doughnut [Fig. 6(d)] to oval, which arises on crossing line 4 in Fig. 5, also amounts to a phenomenon of cylindrical symmetry breaking; it must be kept in mind, however, that the field is not cylindrically symmetrical in the doughnut states.

In conclusion, we have four different kinds of stable patterns: the A_{10} single-mode solution, the doughnut solutions, the 4H solution, and the oval solution. The 4H mode coexists with the two doughnut modes in region D-4H and with the oval mode in region O-4H.

Let us now consider the phase singularities and the equiphase lines of the single-mode stationary solutions. In the case of the doughnut pattern, there is one singularity in the origin, with an associated charge of $+2$ or -2 depending on whether we are dealing with a B_{021} or a B_{022} mode. The equiphase lines of this structure depart radially from the origin and look exactly like the case $2p+l=1$ [Fig. 4(b)]. On the contrary, the A_{10} single-mode solution does not possess any pointlike phase singularity because the field phase does not depend on φ.

The description of the phase singularities in the multiple-mode configurations requires a more detailed analysis. Given a general field of the form (3.16), it is possible to substitute the explicit expression (3.7) for the modal functions so that by combining the two equations $\mathrm{Re}F=0$ and $\mathrm{Im}F=0$ one finds the following pair of equations:

$$\tan(2\varphi)=\frac{\mathrm{Img}_2+\mathrm{Img}_3}{\mathrm{Reg}_3-\mathrm{Reg}_2}\ , \tag{3.19}$$

$$2\rho^2=\frac{\sqrt{2}g_1}{\sqrt{2}g_1-\cos(2\varphi)(\mathrm{Reg}_2+\mathrm{Reg}_3)-\sin(2\varphi)(\mathrm{Img}_3-\mathrm{Img}_2)}\ . \tag{3.20}$$

The solutions of Eq. (3.19) are four angles:

$$\varphi=\bar{\varphi}+k\frac{\pi}{2},\quad k=0,1,2,3\ ,\quad -\frac{\pi}{4}\le\bar{\varphi}\le\frac{\pi}{4}\ . \tag{3.21}$$

In Cartesian coordinates ($x=\rho\cos\varphi$, $y=\rho\sin\varphi$), Eq. (3.21) defines the two perpendicular lines

$$y=\tan(\bar{\varphi})x,\quad y=-\frac{1}{\tan(\bar{\varphi})}x\ .$$

In turn, (3.20) is the equation of a conical centered at the origin. Therefore it is clear that the system formed by Eqs. (3.19) and (3.20) has at most four real solutions, which implies that the maximum number of phase singularities of the degenerate family $2p+l=2$ is four.

Upon substitution of Eq. (3.19) into Eq. (3.20), and taking into account that the condition $\theta_2+\theta_3=\pi$ is always satisfied in the multimode stationary solutions, we obtain the following equation for the distance ρ of the phase singularities from the origin:

$$2\rho_{\pm}^2=\left[1\pm\frac{|g_2|-|g_3|}{\sqrt{2}g_1}\right]^{-1}\ . \tag{3.22}$$

Phase singularities which lie on the same line have the same distance ρ_+ or ρ_- from the origin. The equiphase lines are determined by the equation

$$\tan\Phi=\frac{\mathrm{Im}F}{\mathrm{Re}F}=\frac{(1-2\rho^2)\mathrm{Img}_1+\sqrt{2}\rho^2[\cos(2\varphi)(\mathrm{Img}_2+\mathrm{Img}_3)+\sin(2\varphi)(\mathrm{Reg}_2-\mathrm{Reg}_3)]}{(1-2\rho^2)\mathrm{Reg}_1+\sqrt{2}\rho^2[\cos(2\varphi)(\mathrm{Reg}_2+\mathrm{Reg}_3)+\sin(2\varphi)(\mathrm{Img}_3-\mathrm{Img}_2)]}=\text{const}\ . \tag{3.23}$$

In order to describe the phase singularities and the equiphase lines of the 4H and oval patterns, one has to insert into Eqs. (3.19), (3.22), and (3.23) the modal composition of these two patterns.

Let us consider the 4H solution: since the amplitudes of the two doughnut modes in this pattern are equal, i.e., $|g_2|=|g_3|$, it is a straightforward matter to show from Eqs. (3.22) and (3.19) that the 4H solution has four phase singularities, whose coordinates are

$$\rho_+=\rho_-=1/\sqrt{2},\quad \bar{\varphi}=\frac{\theta_3-\theta_2}{4}+\frac{\pi}{4}\ . \tag{3.24}$$

They are placed on the vertices of a square (Fig. 7), and each of them has a charge equal to either $+1$ or -1; singularities located on the same diagonal have the same sign, so that in this case the crystal is neutral. The equiphase lines show a close resemblance to the lines of the electrostatic field generated by a corresponding set of point charges.

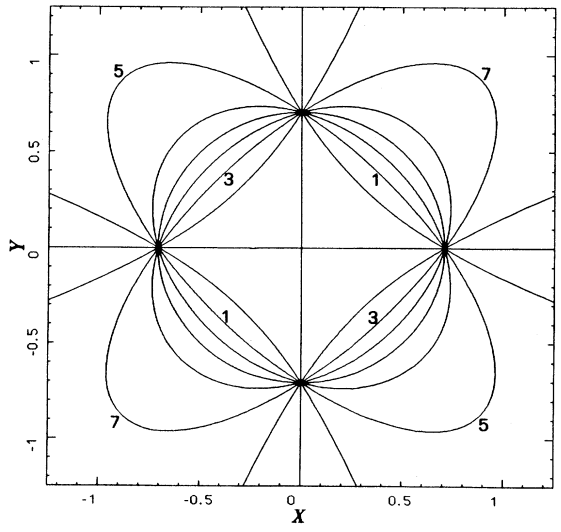

FIG. 7. Equiphase lines for the pattern of Fig. 6(b). $1=\pi/4$, $3=3\pi/4$, $5=5\pi/4$, $7=7\pi/4$.

On the other hand, the oval has only two phase singularities; in fact, condition (3.18) implies that only the equation for ρ_+ admits a solution, the right-hand side of the equation for ρ_- being negative [Eq. (3.22)]. Obviously, the converse is true if one considers an oval with a dominant B_{022} doughnut mode. The charges of the phase singularities are equal in sign, each amounting to $+1$ or to -1 depending on the doughnut contribution which is dominant in the pattern. As in the case of the doughnut modes, the phase singularity array has a net charge of ±2. The equiphase lines display the expected similarity to the lines of the electrostatic field generated by two electric charges of equal sign, as Fig. 8 shows.

We have also performed scans in the parameter space (C,ψ) in order to describe transitions between stable patterns. For example, while keeping ψ constant, one can gradually and slowly sweep C, moving from region D-4H to region S, following the dashed line drawn in Fig. 9,

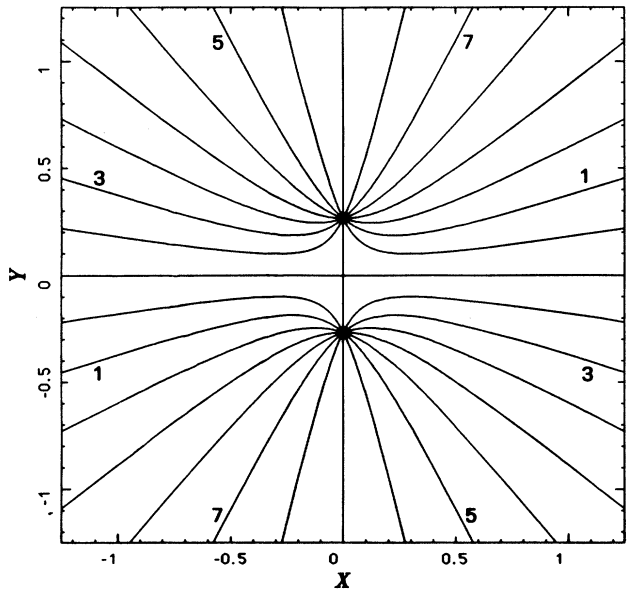

FIG. 8. Equiphase lines for the configuration of Fig. 6(c). $1=\pi/4$, $3=3\pi/4$, $5=5\pi/4$, $7=7\pi/4$.

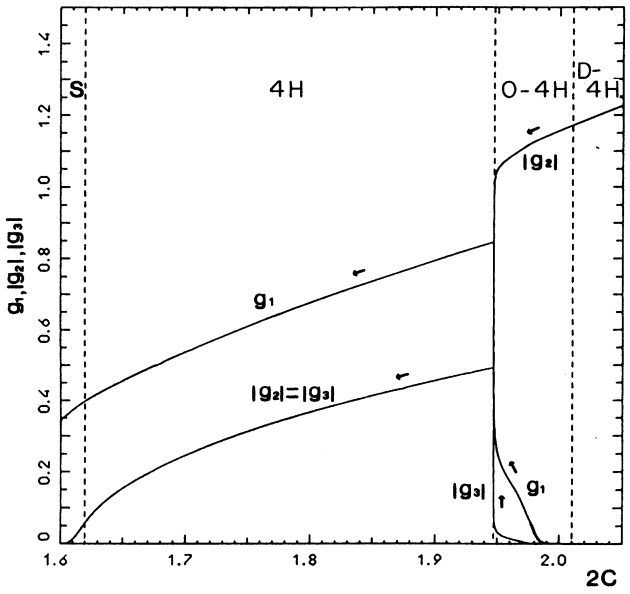

FIG. 10. The pump parameter C is decreased adiabatically from point a to point e in Fig. 9. The lines exhibit the corresponding variation of the moduli of the modal amplitudes.

which is an enlargement of a part of Fig. 5. We started from a doughnut pattern which is stable in region D-4H, and observed first the continuous transition to the oval solution, then the discontinuous transition to the 4H solution, and eventually the continuous transition to the A_{10} single-mode solution.

Figure 10 displays the evolution of the quasi-steady-state values of the modal amplitudes g_1, $|g_2|$, and $|g_3|$ as the system passes from point a to point e of Fig. 9. Initially, only the component $|g_2|$ relative to the doughnut mode B_{022} is present. Abandoning region D-4H causes the growth of g_1 and $|g_3|$, that is, the transition to the oval pattern. The oval pattern, in turn, becomes unstable at point d in Fig. 9, which corresponds to the condition

$$\sqrt{2}g_1=|g_2|-|g_3| \ , \tag{3.25}$$

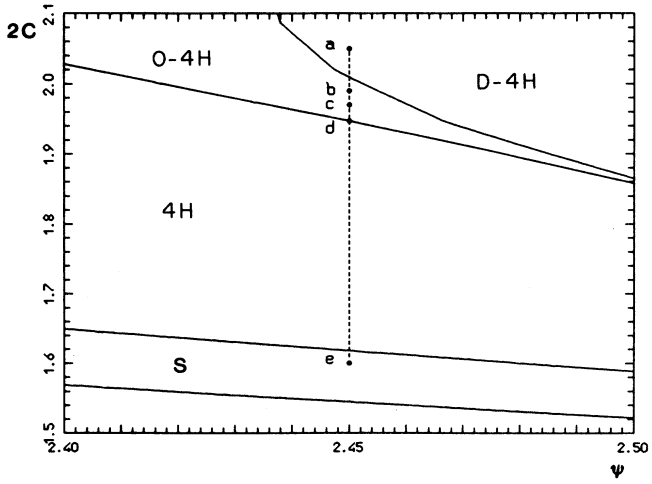

FIG. 9. Enlarged view of a part of Fig. 5. As for the points $a-e$ see the text.

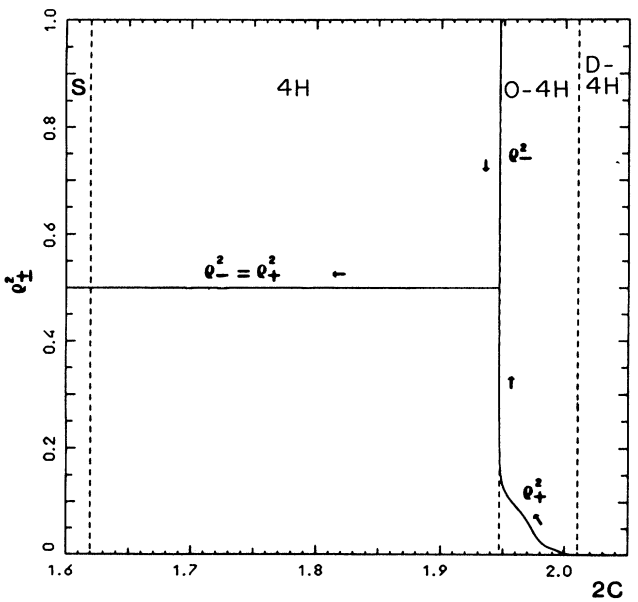

FIG. 11. The pump parameter C is decreased adiabatically from point a to point e in Fig. 9. The lines indicate the corresponding variation of the square distances of the phase singularities from the origin.

and the system jumps to the 4H configuration, with $|g_2|=|g_3|$. Continuing to decrease C, the doughnut components become smaller and smaller, until we enter region S, where only g_1 survives.

The meaning of the instability threshold (3.25) for the oval pattern becomes clear, if we analyze the motion of the phase singularities. This is described by the corresponding evolution of ρ_+ and ρ_- shown in Fig. 11. First of all, as we said, for small values of g_1, only the equation for ρ_+ has a solution [Eq. (3.22)], whose value is zero when g_1 vanishes (pure doughnut mode) and increases with g_1. This explains the splitting of the double-charge phase singularity associated with the doughnut mode into the two phase singularities of unitary charge of the oval and their progressive separation, as shown in Fig. 12, where we plotted the transverse profile of $|F|$ for values of $2C$ corresponding to points a, b, and c in Fig. 9. Equation (3.25) is just the threshold condition for the existence of a solution ρ_-. In the condition defined by Eq. (3.25), two new phase singularities appears at infinity, with a charge opposite to that of the singularities of the oval mode. This causes the destabilization of the oval mode,

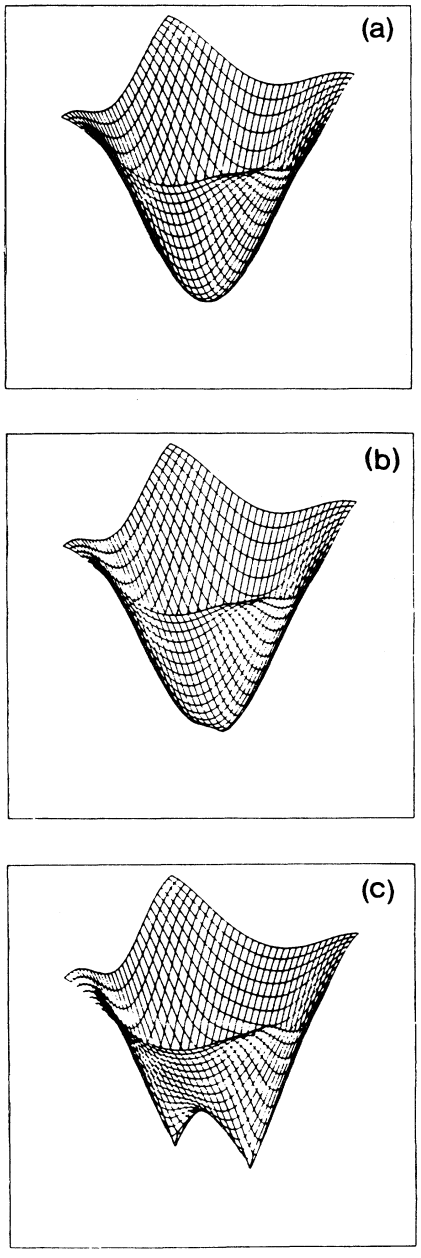

FIG. 12. Transverse intensity distribution for the inner part of the spatial pattern. Graphs (a), (b), and (c) correspond, respectively, to points a, b, and c in Fig. 9.

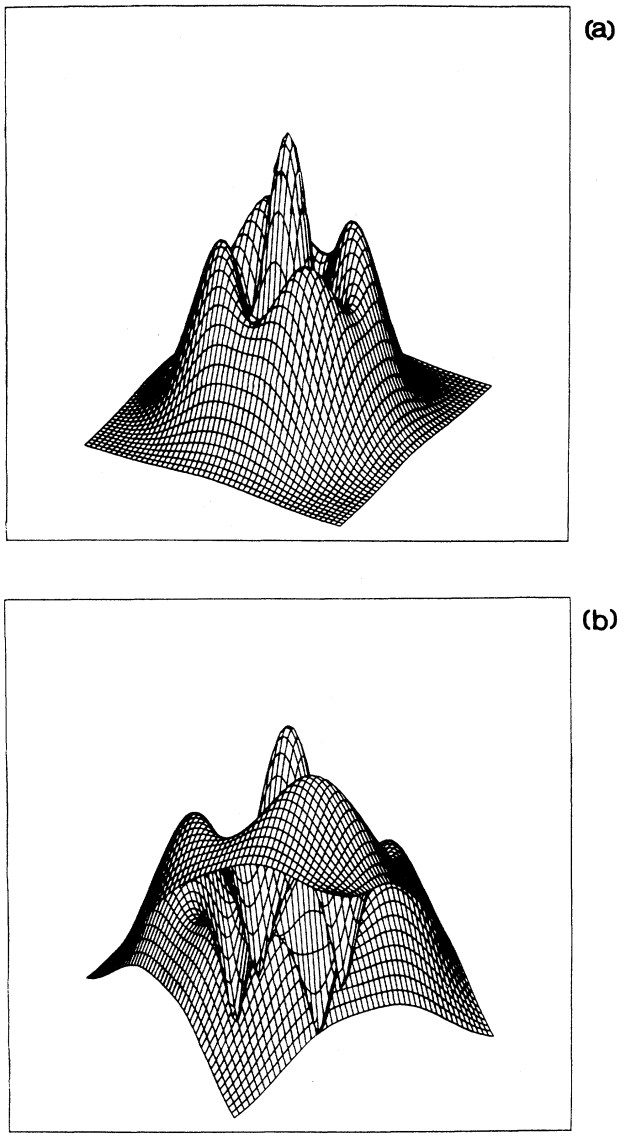

FIG. 13. Transverse distribution of the modulus of the electric field for the 4H pattern. (a) Top view; (b) bottom view.

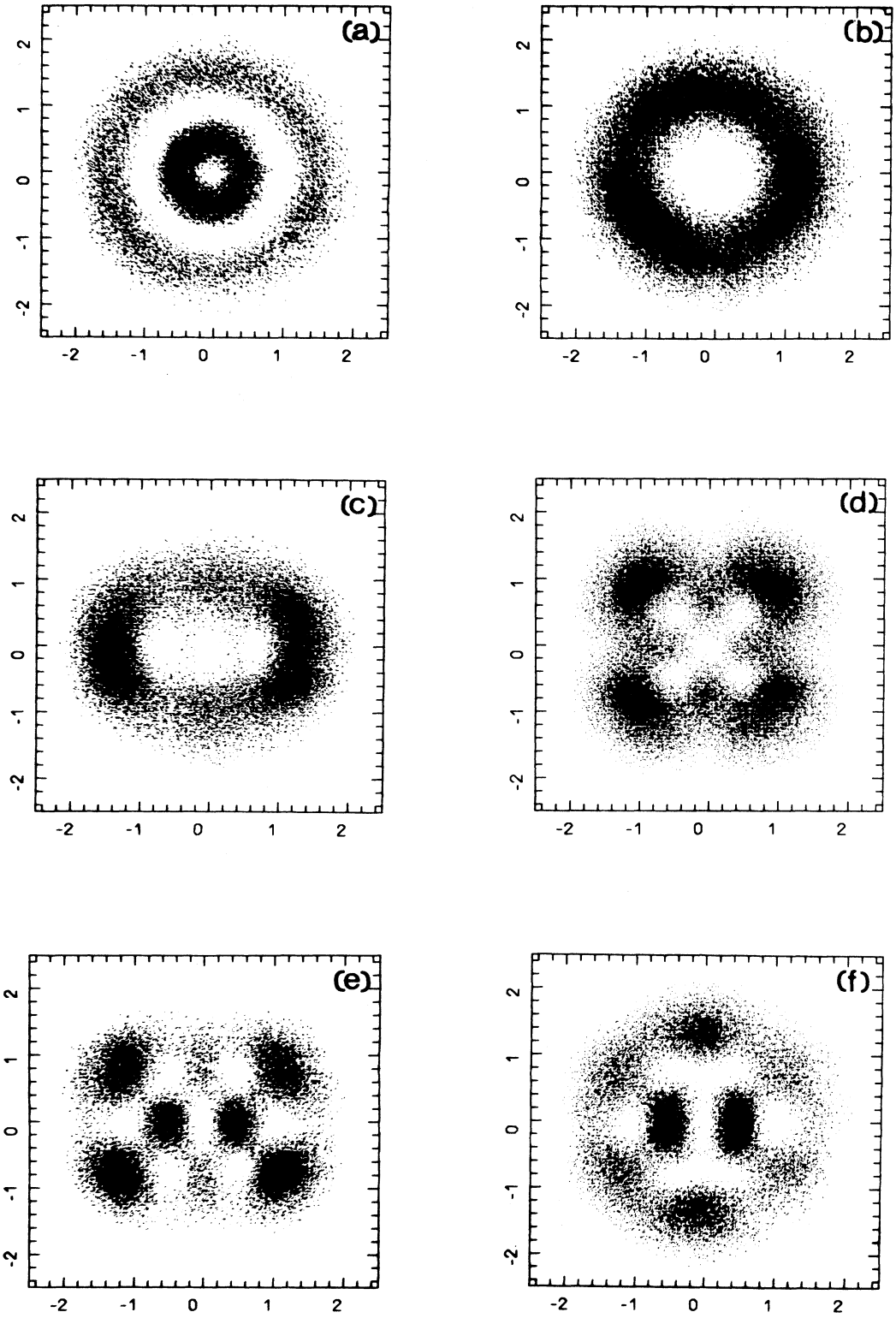

FIG. 14. Case $2p+l=3$, stable patterns. Black areas indicate high local light intensity. (a) Doughnut pattern, $p=1$, $l=1$; (b) doughnut pattern, $p=0$, $l=3$; (c), (d), (e), and (f) show the patterns with 3, 5, 7, and 9 phase singularities, respectively.

and the four phase singularities arrange themselves in such a way that they form the crystal associated with the 4H solution, with $\rho_+=\rho_-=1/\sqrt{2}$. Thus, the oval-4H transition is discontinuous.

If we perform the same sweep on the parameter C but in the opposite direction, we find only the transition from the A_{10} single-mode solution to the 4H solution, as predicted theoretically in Ref. 23 and observed experimentally.[28] This means that it is possible to have hysteresis among the 4H, the oval, and the doughnut patterns.

Finally, Fig. 13 shows a view of $|F|$ for the 4H pattern from below. We see the presence of four inverted cones centered at the phase singularities, and we note the similarity of these structures with the case of optical vortices, as it appears from the comparison with Figs. 4 and 5(a) of Ref. 33.

C. The case $2p+1=3$

In this case the nondegenerate family consists of the four modes

$$B_{111}(\rho,\varphi)=\frac{1}{\sqrt{\pi}}(2\rho^2)^{1/2}(2-2\rho^2)e^{-\rho^2}e^{+i\varphi}\ , \tag{3.26a}$$

$$B_{112}(\rho,\varphi)=\frac{1}{\sqrt{\pi}}(2\rho^2)^{1/2}(2-2\rho^2)e^{-\rho^2}e^{-i\varphi}\ , \tag{3.26b}$$

$$B_{031}(\rho,\varphi)=\frac{1}{\sqrt{\pi}}\frac{(2\rho^2)^{3/2}}{\sqrt{3}}e^{-\rho^2}e^{+3i\varphi}\ , \tag{3.26c}$$

$$B_{032}(\rho,\varphi)=\frac{1}{\sqrt{\pi}}\frac{(2\rho^2)^{3/2}}{\sqrt{3}}e^{-\rho^2}e^{-3i\varphi}\ . \tag{3.26d}$$

The single-mode steady-state equation for the first pair of doughnut modes B_{11i} $(i=1,2)$ reads

$$1=2C\int_0^\infty d\rho 4\rho\frac{\rho^2(2-2\rho^2)^2e^{-2\rho^2}}{1+\rho^2(2-2\rho^2)^2e^{-2\rho^2}x_{1,2}^2}\chi(\rho)\ , \tag{3.27}$$

while the stationary equation for the other pair B_{03i} $(i=1,2)$ is

$$1=2C\int_0^\infty d\rho 4\rho\frac{(2\rho^2)^3e^{-2\rho^2}}{6+(2\rho^2)^3e^{-2\rho^2}x_{3,4}^2}\chi(\rho) \tag{3.28}$$

where x_i are the scaled amplitudes

$$x_i=\begin{cases}\left[\dfrac{2}{\pi}\right]^{1/2}|g_{11i}|, & i=1,2\\ \left[\dfrac{2}{\pi}\right]^{1/2}|g_{03(i-2)}|, & i=3,4\ .\end{cases} \tag{3.29}$$

The intensity patterns of these solutions are shown respectively in Figs. 14(a) and 14(b). The threshold for the B_{11i} solutions is

$$2C_{\rm thr}^{(11i)}=\frac{(\psi^2+1)^4}{\psi^4(\psi^4+2)}\ , \tag{3.30}$$

while for the B_{03i} solutions the threshold is

$$2C_{\rm thr}^{(03i)}=\frac{(\psi^2+1)^4}{\psi^8}\ . \tag{3.31}$$

It is easy to verify that $2C_{\rm thr}^{(11i)}\le 2C_{\rm thr}^{(03i)}$; again the equality holds in the limit $\psi\to\infty$.

The linear stability analysis of the doughnut states is more complicated than in the previous case $2p+l=2$ because of the coupling between the modes; the instability conditions for each pair of doughnut modes are

$$[(I_1-I_2)^2+4I_3^2]^{1/2}+I_1+I_2-2>0\ , \tag{3.32}$$

where

$$I_1=2C\int_0^\infty d\rho 4\rho\frac{\rho^2(2-2\rho^2)^2e^{-2\rho^2}}{[1+\rho^2(2-2\rho^2)^2e^{-2\rho^2}x_{1,2}^2]^2}\chi(\rho)\ , \tag{3.33a}$$

$$I_2=2C\int_0^\infty d\rho\frac{2}{3\sqrt{3}}\rho\frac{(2\rho^2)^3e^{-2\rho^2}}{[1+\rho^2(2-2\rho^2)^2e^{-2\rho^2}x_{1,2}^2]^2}\chi(\rho)\ , \tag{3.33b}$$

$$I_3=2C\int_0^\infty d\rho\rho\frac{(2\rho^2)^3(2-2\rho^2)^3e^{-4\rho^2}}{[1+\rho^2(2-2\rho^2)^2e^{-2\rho^2}x_{1,2}^2]^2}\times\chi(\rho)x_{1,2}^2\ , \tag{3.33c}$$

for the B_{11i} solutions, and

$$2C\int_0^\infty d\rho 4\rho\frac{36\rho^2(2-2\rho^2)^2}{[6+(2\rho^2)^3e^{-2\rho^2}x_{3,4}^2]^2}e^{-2\rho^2}\chi(\rho)>1 \tag{3.34}$$

for the B_{03i} solutions.

In addition to the doughnut states which we found analytically, there exist other four stable stationary states, which are linear combinations of the modes (3.26). The intensity patterns of these solutions are shown in Figs. 14(c)–14(f). We call these three-hole (3H), five-hole (5H), seven-hole (7H), and nine-hole (9H) patterns, respectively.

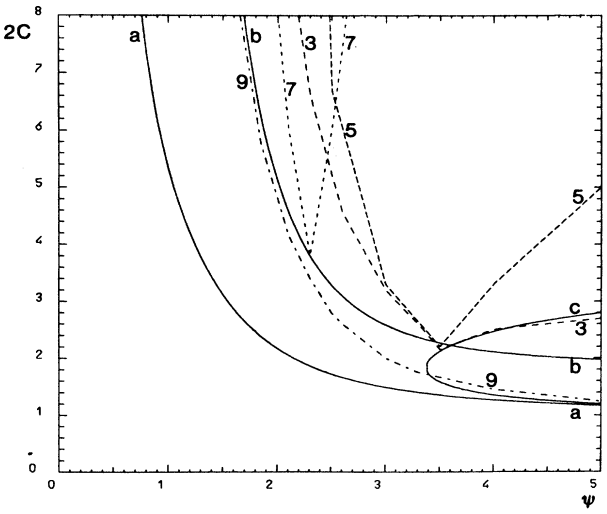

FIG. 15. Case $2p+l=3$. Phase space diagram in the plane of the control parameters C and ψ. The diagram indicates the domain of existence of the patterns shown in Fig. 14 (see text).

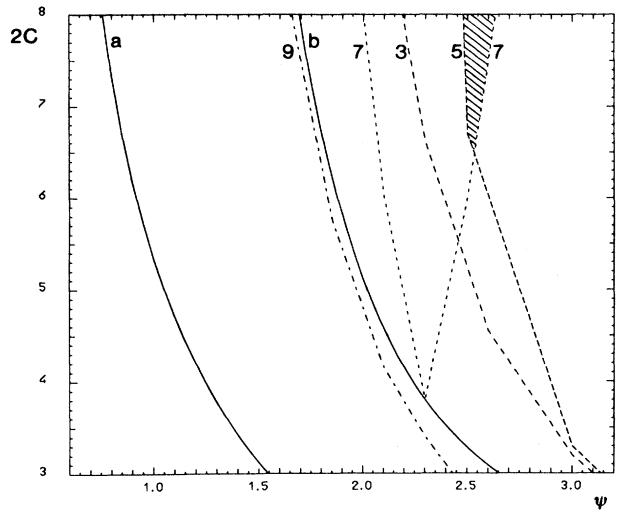

FIG. 16. Magnified view of a portion of Fig. 15. In the shaded region, the pattern with 3, 5, 7, and 9 singularities coexist.

For these states the stability domains have been investigated numerically, spanning the control parameter plane; the results of this investigations are shown in Figs. 15 and 16. In these figures we plotted the stability boundaries for all known stable patterns. The stability domain of the doughnut B_{11i} modes is enclosed between lines a and b, while the doughnut B_{03i} modes are stable in the region enclosed in line c. These three lines are, respectively, the graphical representations of Eqs. (3.30), (3.32), and (3.34), with the greater than sign replaced by an equal sign.

The stability domains of the 3H, 5H, 7H, and 9H patterns are the regions above the dashed lines with the numbers 3, 5, 7, and 9, respectively. It is worth noting that there are regions where up to four different patterns coexist; see especially the shaded region in Fig. 16, where four patterns coexist. In analogy with the $2p+l=2$ case, in all the multimode stable solutions, the sum of the phases of the complex amplitudes of the four modes (3.26) is equal to π.

As for the phase singularities, we note that the doughnut B_{11i} and B_{03i} patterns have one singularity at the origin, having charges ± 1 and ± 3, respectively, while the 3H, 5H, 7H, and 9H patterns show 3, 5, 7, and 9 singularities, respectively, each of unitary charge, arranged in the form of regular crystals. The total charge is ± 3, ± 3, ± 1, and ± 1, respectively. Figures 17(a)–17(c) show the equiphase lines for three stable patterns of Fig. 14. The similarity with the lines of the electrostatic field generated by the corresponding set of pointlike charges is once again evident.

IV. POINTLIKE VORTEX STRUCTURE OF THE ELECTRIC-FIELD PHASE SINGULARITIES

The numerical solution of Eqs. (2.8) describing the time evolution of the laser has shown the onset of nontrivial spatial structures of the electric field characterized by the presence of singularities in the electric phase. In this section we thoroughly examine the nature of these singular configurations, showing that the order parameter field Ψ describing two-dimensional pointlike vortex configurations for a fluid is concealed in the complex-valued function representing the electric field, and gives rise to the phase singularities.

Let us first review the analytic description of a two-dimensional, compressible, rotational fluid.[30,31] Let $\mathbf{v}(\mathbf{r})$

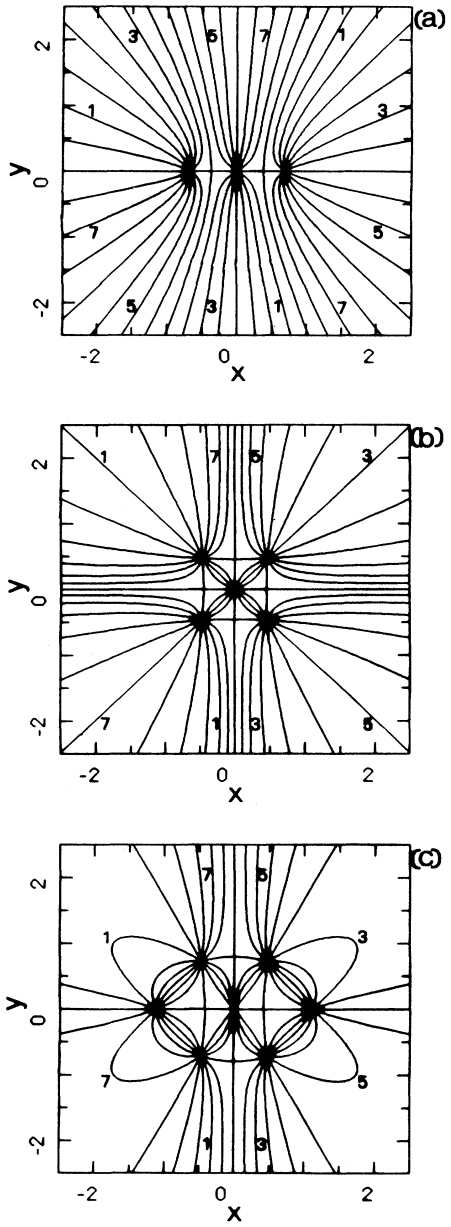

Fig. 17. Equiphase lines for three stable patterns in the case $2p+l=3$. (a), (b), and (c) correspond to Figs. 14(c), 14(d), and 14(e), respectively. $1=\pi/4$, $3=3\pi/4$, $5=5\pi/4$, $7=7\pi/4$.

be the velocity field; $\mathbf{v}$ is assumed to be rapidly vanishing at infinity for consistency with the fact that fluids have finite extension. For the sake of comparison with the laser case, we consider a Cartesian orthonormal basis $\{\mathbf{e}_x,\mathbf{e}_y,\mathbf{e}_z\}$ and we assume that $\mathbf{v}$ is two dimensional, i.e., $\mathbf{v}=v_x\mathbf{e}_x+v_y\mathbf{e}_y$ with v_x,v_y independent of z.

For a fluid the compressible condition is

$$\nabla\cdot\mathbf{v}=\partial_x v_x+\partial_y v_y\neq 0 , \tag{4.1}$$

whereas the rotational condition is

$$\nabla\times\mathbf{v}=e_z(\partial_x v_y-\partial_y v_x)\neq\mathbf{0} . \tag{4.2}$$

Equations (4.1) and (4.2) imply that $\mathbf{v}$ can be represented as a sum of an irrotational term and a divergenceless term:

$$\mathbf{v}=\nabla\eta+\nabla\times\mathbf{A} , \tag{4.3}$$

where $\eta=\eta(x,y)$ and $\mathbf{A}$ has the form

$$\mathbf{A}=\mathbf{e}_z A(x,y) . \tag{4.4}$$

Hence using the identity $\nabla\times\nabla\times\mathbf{A}=\nabla(\nabla\cdot\mathbf{A})-\nabla^2\mathbf{A}$ one obtains

$$\nabla\cdot\mathbf{v}=\nabla\cdot\nabla\eta=\nabla^2\eta\neq 0 , \tag{4.5}$$

$$\nabla\times\mathbf{v}=\nabla\times\nabla\times\mathbf{A}=-\nabla^2\mathbf{A}\neq 0 , \tag{4.6}$$

which show that the compressibility and irrotationality of the fluid are described by the *scalar potential* η and the *vector potential* $\mathbf{A}$, respectively. The quantity $\nabla\times\mathbf{v}$ is the *vorticity field* of the fluid and is denoted by $\mathbf{w}$, whereas $\nabla^2\eta$ describes the distribution of sources and wells in the space and represents the hydrodynamical counterpart of the charge distribution in electrostatics. On the other hand, the condition (4.6) has no electrostatic counterpart, since the electric field is irrotational. The circulation of $\mathbf{v}$ along a loop γ in the plane (x,y) is directly connected with $\mathbf{w}$ through the Stokes theorem:

$$\mathcal{C}_\gamma=\oint_\gamma\mathbf{v}\cdot d\mathbf{l}=\int\int_{S_\gamma}\mathbf{w}\cdot d\mathbf{S}\quad(d\mathbf{S}\equiv\mathbf{e}_z dxdy) , \tag{4.7}$$

where S_γ is the region of the (x,y) plane contained in γ; $\mathcal{C}_\gamma$ describes the rotational activity of the fluid in the region S_γ, i.e., the vorticity in S_γ. Therefore, $\mathbf{w}$ represents the density of vorticity of the field $\mathbf{v}$ in the plane. Let us specialize the above discussion to the case when $\mathbf{w}$ is a distribution such that $\nabla^2\mathbf{A}$ is a sum of Dirac δ functions. In this case $\mathbf{w}$ is nonzero in a discrete set of points in the plane that corresponds to the points where the δ functions are centered. Now, recalling that the Green function on a plane

$$\mathcal{G}=\frac{1}{4\pi}\ln[(x-x_0)^2+(y-y_0)^2] \tag{4.8}$$

satisfies the equation[38]

$$\nabla^2\mathcal{G}=\delta^{(2)}(\mathbf{r}-\mathbf{r}_0)=\delta(x-x_0)\delta(y-y_0) ,$$

the solution of the equation

$$-\nabla^2 A=\sum_j q\,m_j\delta^{(2)}(\mathbf{r}-\mathbf{r}_j) , \tag{4.9}$$

where q is a positive real factor with the dimensions of the vorticity and m_j is a positive or negative integer, is easily found to be

$$A(\mathbf{r})=-\sum_j m_j\frac{q}{4\pi}\ln|z-z_j|^2\equiv-\frac{q}{2\pi}\alpha(\mathbf{r}) , \tag{4.10}$$

where $z=x+iy$, $z_j=x_j+iy_j$. We remark that the coefficients m_j are required to be integers in order to ensure the single-valued state of the order parameter field Ψ—which we shall introduce later—over the x-y plane.

The most interesting feature of the scalar field α is that it can be seen as the real part of the analytic function

$$f(z)=\sum_j m_j\ln(z-z_j) . \tag{4.11}$$

The points $z=z_j$ are branching points of $f(z)$. This immediately follows by observing that the imaginary part of f is

$$\beta=\mathrm{Im}f=\sum_j m_j\Phi_j,\quad\Phi_j\equiv\tan^{-1}\frac{y-y_j}{x-x_j} , \tag{4.12}$$

where each phase Φ_j is, of course, a multivalued function. Therefore Φ_j is singular for $z=z_j$ in the sense that it is increased by $2\pi k$ whenever one goes around the point z_j k times. Φ_j's equiphase lines are identical to those shown in Fig. 4.

The correspondence between the phase singular points and the velocity field singular points, where the vorticity is nonzero, is established as follows. Since f is analytic for each $z\neq z_j$, we have the Cauchy conditions

$$\partial_x\alpha=\partial_y\beta,\quad\partial_y\alpha=-\partial_x\beta , \tag{4.13}$$

which connect the real part α with the imaginary part β of f. This is equivalent to the vector equation [see Eqs. (4.4) and (4.10)]

$$\nabla\beta=-\nabla\times(\mathbf{e}_z\alpha)=\frac{2\pi}{q}\nabla\times\mathbf{A} . \tag{4.14}$$

Now, with the help of Eqs. (4.3) and (4.14), the velocity field associated with a pointlike vortex configuration is given by

$$\mathbf{v}=\nabla\eta+\frac{q}{2\pi}\nabla\beta , \tag{4.15}$$

which, by using Eq. (4.12), reads

$$\mathbf{v}=\nabla\eta+\frac{q}{2\pi}\sum_j m_j\nabla\Phi_j$$

$$=\nabla\eta-\frac{q}{2\pi}\sum_{j=1}^{N}m_j\left[\frac{(y-y_j)\mathbf{e}_x-(x-x_j)\mathbf{e}_y}{(y-y_j)^2+(x-x_j)^2}\right] , \tag{4.16}$$

with $|\mathbf{v}|\to\infty$ at the phase singular points $z=z_j$. Taking into account Eq. (4.15), the vorticity in a region S_γ will be

$$C_\gamma=\oint_\gamma\mathbf{v}\cdot d\mathbf{l}=\frac{q}{2\pi}\oint_\gamma\nabla\beta\cdot d\mathbf{l} , \tag{4.17}$$

where one can show, by a direct calculation using Eq. (4.16), that

$$\oint_\gamma \nabla\beta \cdot d\mathbf{l} = 2\pi \sum_j{}' m_j \ . \tag{4.18}$$

The prime on the summation indicates that only the singular points encircled by γ contribute. Notice that $\mathcal{C}_\gamma$ could be also obtained from (4.7) by simply expressing $\mathbf{w}$ through (4.9). Nevertheless, (4.17) and (4.18) are meaningful, since they make transparent the connection between the presence of vortices and the fact that $\nabla\beta$ is a pseudogradient [as shown by (4.18)], because the phase β is a multivalued function. A further reason for describing $\mathbf{v}$ in the form (4.15) is that one can easily recover the description of a fluid in terms of the order parameter field, which is usual for statistical systems. In fact, upon introducing the field

$$\Psi = |\Psi| e^{i\Phi}, \quad \Phi = \lambda + \beta \ , \tag{4.19}$$

where

$$\lambda = \frac{2\pi\eta}{q} \ , \tag{4.20}$$

so that, using Eq. (4.15),

$$\mathbf{v} = \frac{q}{2\pi} \nabla\Phi \ , \tag{4.21}$$

$\mathbf{v}$ can be expressed in the $|\Psi|^2$-independent form

$$\mathbf{v} = \frac{q}{4\pi i |\Psi|^2} (\Psi^* \nabla\Psi - \Psi \nabla\Psi^*) \ . \tag{4.22}$$

The formula (4.22) is well known in the condensed-matter physics of systems with topological defects, where Ψ is the *order parameter field* describing the physical state of the system at each point of the medium. In particular, for superfluids and superconductors,[39] (4.22) gives the local average velocity of ^{4}He superfluid atoms and the local velocity (up to the magnetic potential vector) of the frictionless charges in the eddy supercurrents, respectively, whereas in the case of the magnetic spin system, $\mathbf{v}$ is to be understood as the local magnetization.[29]

All these systems are endowed with defects that are pointlike vortices and correspond to the singularities of β, just as in the case of the vortex model formulated above. The remaining degrees of freedom of Ψ, namely $|\Psi|$ and the single-valued part η of Φ depend on the system which one is dealing with, but do not concern the description of defects. For example, superfluids are assumed to be divergenceless fluids with constant mass density; this involves the conditions $\nabla \cdot \mathbf{v} = \nabla^2 \eta = 0$, i.e., $\eta = 0$, and $|\Psi|^2 = \text{const}$.

The naive fluid model with vorticity also allows us to describe the phase singularities of the complex electric field F and leads us to regard F as the order parameter field, as is usual.[7] In order to show this, let us consider F in the case that N singularities are embodied in the phase. Such singularities are characterized by the fact that the equiphase lines arise from isolated points, thus causing them to be quite similar to the hydrodynamical ones in some neighborhood of these points. The comparison of Fig. 7 with Fig. 18 makes such a similarity manifest. Hence it is quite natural to put the field F in the form

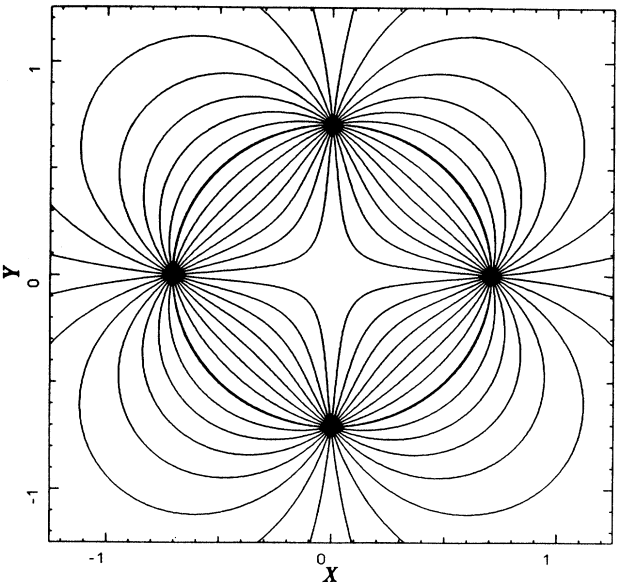

FIG. 18. Equiphase lines for the field $|F|\exp(i\beta)$, with β given by Eq. (4.12), and the phase singularities are the same as in Fig. 7. This figure shows the difference between the equiphase lines of the electric field (Fig. 7) and those of the simple hydrodynamical model with vortices, considered in Sec. IV.

$$F = |F| e^{i\Phi}, \quad \Phi = \lambda + \beta \ , \tag{4.23}$$

where β is defined as

$$\beta = \beta_+ - \beta_- \ , \tag{4.24}$$

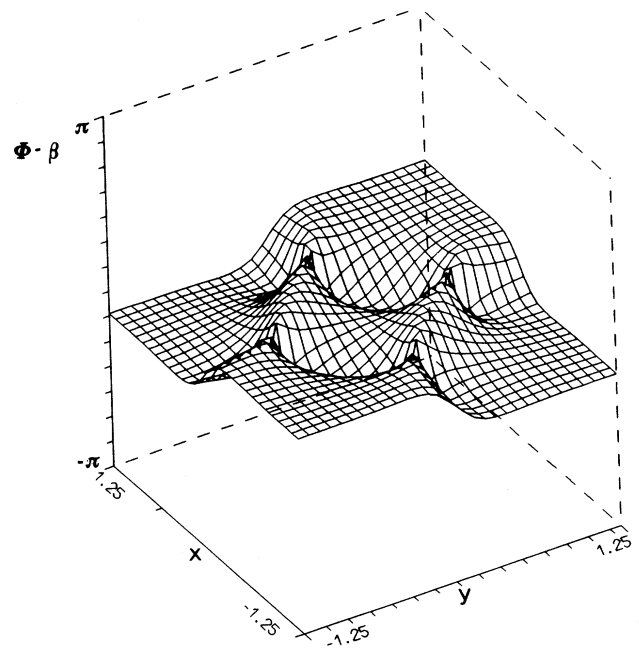

FIG. 19. Plot of the quantity $\lambda = \Phi - \beta$ (see text).

with

$$\beta_{\pm}=\sum_{j=1}^{N_{\pm}} m_j^{\pm}\tan^{-1}\left[\frac{y-y_j^{\pm}}{x-x_j^{\pm}}\right], \quad m_j^{\pm}>0 \tag{4.25}$$

and the coordinates $(x_j^{\pm},y_j^{\pm})$ are the phase singularity points obtained from the equations $\mathrm{Re}F=0$ and $\mathrm{Im}F=0$, m_j^{+} are the topological charges of the N_+ positively charged singularities and m_j^{-} are the moduli of the N_- negatively charged singularities.

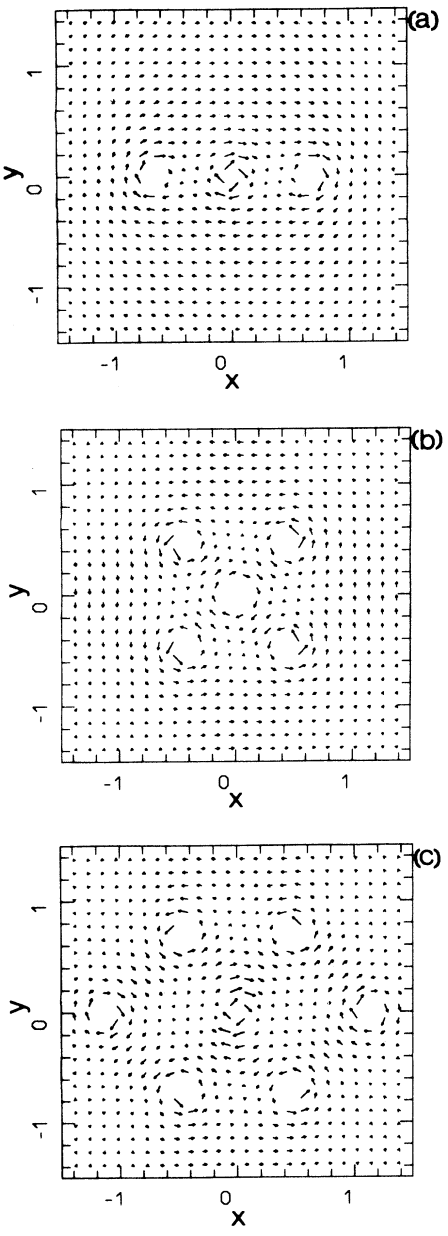

FIG. 20. Behavior of the field $\nabla\Phi\propto\mathbf{v}$ in correspondence to the three patterns shown in Figs. 14(c), 14(d), and 14(e), respectively. The arrows indicate the direction of the field $\nabla\Phi$ in each point; the length of the arrow is proportional to $|\nabla\Phi|$, i.e., to $|\mathbf{v}|$.

As an example, we can consider the 4H configuration described in Sec. III, where Φ is given by Eq. (3.23), $N_+=N_-=2$, and $(x_j^{\pm},y_j^{\pm})$, $j=1,2$ are fixed by Eq. (3.24). Figure 19 shows the difference between Φ and the topological phase β defined by Eqs. (4.24) and (4.25) for the 4H configuration: one can see that $\Phi-\beta$ is topologically trivial, in the sense that all phase singularities disappear. Then the role played by the factor $|F|e^{i\lambda}$ is the following: since $e^{i\beta}$ contains all the information concerning the phase singularities, then $e^{i\lambda}$ simply represents the "deformation" which connects the electric-field phase Φ to the pure topological term β. λ is trivial because the circulation of $\nabla\lambda$ (a true gradient involving the compressible condition) is vanishing everywhere.

The further factor $|F|$ ensures the exponential decay of the electric field out of the core of the laser beam, and it is characterized by the fact that its zeros just coincide with the phase singularity points.

We conclude by observing that indeed the optical defects that we discovered have the same analytic structure of pointlike vortices and, upon assuming F as the order parameter field of the laser, it is possible to get all the relevant hydrodynamical quantities such as $\mathbf{v}$, $\mathbf{w}$, etc. for our optical fluid. In the final section of a companion paper,[40] we stress further this parallelism by reducing the time-evolution equation for F to a pair of hydrodynamical equations; this also allows us to fix the parameter q for the optical fluid. Leaving for the moment the proportionality constant q unspecified, we plot in Fig. 20 the field $\nabla\Phi\propto\mathbf{v}$ for the patterns shown in Figs. 14(c), 14(d), and 14(e), respectively.

V. EXPERIMENT

In the following we describe an experimental study on the transverse radiation patterns of a traveling-wave laser which operates under conditions where various families of frequency-degenerate transverse resonantor modes can be excited selectively. The gain medium of the laser consists of sodium dimer (Na_2) vapor, optically pumped in a three-level configuration by an argon-ion laser. One of the main characteristics of this type of laser is the velocity-selective optical excitation of the Doppler-broadened molecular vapor by the pump laser, which strongly favors oscillation in a traveling wave copropagating with pump field.[41] Another consequence of the narrow-linewidth optical excitation is that under typical experimental conditions, the free spectral range of the laser resonator is significantly larger than the linewidth of the lasing transition. This implies that Na_2 lasers usually oscillate in a single longitudinal mode.

The narrow gain line of a Na_2 laser allows us to selectively excite various higher-order transverse-mode resonances of the laser resonator by tuning their eigenfrequencies into resonance with the gain medium. The experimental system described below makes use of this fact and permits us to study the field patterns formed by the individual families of frequency-degenerate Gauss-

Laguerre transverse modes TEM_{pl} of order $2p+l=q=1$, 2, or 3, while transverse modes of higher order are suppressed by an intracavity aperture. With respect to the selective excitation of groups of cavity modes of equal transverse order, our experiment thus realizes a situation very similar to the one considered in theoretical part of this paper.

In our experiment, the optical ring resonator of the laser supports the Gauss-Laguerre transverse modes of a cylindrically symmetric linear cavity because the astigmatic aberrations of the various optical elements of the resonator compensate each other. The experimental setup nevertheless must be expected to deviate to some extent from a perfect cylindrical symmetry because it is subject to perturbations like air currents, residual misalignments of resonator and pumping geometry, and optical imperfections. The mathematical description given in Secs. II–IV allows no predictions on the effects of such perturbations on the stability of the expected field patterns and phase singularity structures, since for the sake of clarity it assumes an optical system of perfect cylindrical symmetry. One of the main objectives of our experimental study was to test the validity of the theoretical model of Secs. II–IV under the realistic condition of imperfect cylindrical symmetry of the optical system.

A. Experimental setup

The experimental setup is shown in Fig. 21. The sodium-dimer vapor laser is collinearly pumped by the approximately Gaussian output beam of a single-frequency $\lambda=488$ nm argon-ion laser. The collimated pump beam is superimposed with the intracavity field by means of a Brewster prism which also selects one particular molecular transition of the Na_2 molecule as the lasing transition. The pump laser was tuned to the center of the Doppler-broadened $(6,43)X\,{}^1\Sigma_g^+-(3,43)B\,{}^1\Pi_u$ transition

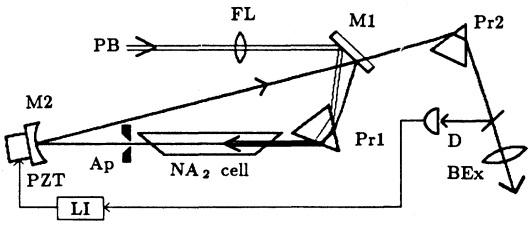

FIG. 21. Experimental setup. The output beam PB of the pump laser is collimated by focusing lens FL (focal length 0.5 m) whose distance to the Na_2 cell can be varied (see text). The laser ring resonator is formed by plane outcoupling mirror $M1$ (power transmission 2%) and high-reflecting concave (radius of curvature 0.713 m) mirror $M2$; Pr1: intracavity Brewster prism; Ap: iris aperture. The Brewster prism Pr2 separates the laser output from the transmitted part of the pump field. BEx is a beam expansion lens. Detector D, Lock-in circuit LI and piezoelement PZT form a servo loop locking the selected higher-order transverse-mode resonance of the resonator (see text) to the peak of the gain line of the laser medium.

of Na_2. At a temperature of the sodium heat-pipe cell of approximately 700 K and a helium buffer gas pressure of 10 mbar, approximately 70% of the pump laser power was absorbed in the 40-mm-long Na_2 vapor zone. As a lasing transition with relatively high gain at low pump intensities, the $\lambda=525$ nm ($Q13$) transition from the upper level of the pump transition was selected by the intracavity prism.

The transmission of the outcoupling mirror and absorption losses in the gain medium together led to a total loss coefficient for the intracavity field per round-trip of $\kappa\mathcal{L}/c\approx 0.05$. Typical pump intensity values for laser threshold were in the range of 0.01–0.2 W/mm^2, with the actual value depending on the selected transverse-mode resonance of the cavity and on the degree of collimation of the pump beam. The resonator losses were sufficiently small to obtain comparable intensities of intracavity and pump field for pump levels well above the lasing threshold. An approximately linear variation of the laser output power with pump power was observed in the experimentally studied pump intensity range of less than 2 W/mm^2. Under these conditions, the gain resonance line of the Na_2 laser is expected to be approximately Lorentzian with a width mainly determined by the collisional relaxation between the lower levels of the pump and laser transitions.[41] The linewidth of the lasing transition was $\gamma_\perp/2\pi\approx 50$ MHz. Traveling-wave operation in a single longitudinal mode was obtained under all operating conditions which were studied. As a result of the Brewster-angle optical surfaces inside the cavity, the polarization of the laser output was constant and uniform over the beam cross section.

As shown in Fig. 21, the optical ring resonator of the Na_2 laser uses one concave and one plane mirror. The free spectral range of the resonantor is $c/\mathcal{L}\approx 420$ MHz. The optical round-trip path $\mathcal{L}$ in the cavity is equal within ± 2 mm to the radius of curvature r of the concave mirror. The resonance conditions for higher-order transverse modes in this ring resonator are equivalent to those of a linear cavity with the plane and the concave mirror spaced by $2\mathcal{L}=r$. As a result, the eigenfrequencies of the families of Gauss-Laguerre modes TEM_{pls} of transverse order $2p+l=q$ ($q=1,2,3$) are equally spaced between the TEM_{00} resonances of subsequent longitudinal orders s.[42] If the emission of higher-order transverse modes with $q>3$ is suppressed (see below), the families of Gauss-Laguerre modes of order $q=1$, 2, or 3 can be excited selectively by tuning their eigenfrequencies into resonance with the gain medium (see Fig. 22). A particular feature of this quasisemiconfocal cavity configuration is that transverse modes of higher order $2p+l=4k+q$ ($k=1,2,\ldots$) and longitudinal order $s-k$ are frequency degenerate with those of transverse order $2p+l=q$ ($q=1,2,3$) and longitudinal index s. An emission of field patterns formed by the corresponding sets of degenerate transverse modes of different longitudinal and transverse orders can be expected if higher-order transverse modes are not suppressed by a suitable intracavity aperture. In order to permit a straightforward comparison with the theoretical results, most of the experimental observations described in the following were made with a circular

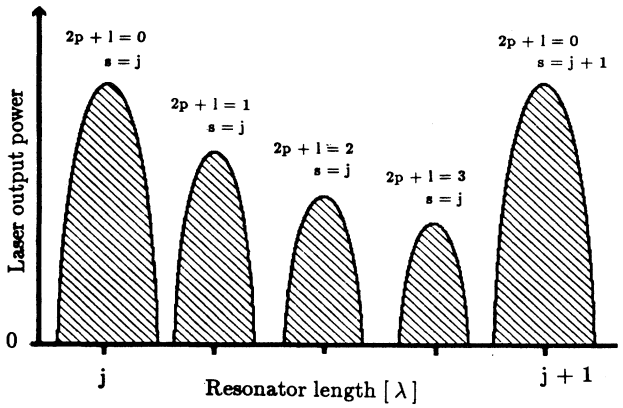

FIG. 22. Sketch of the tuning characteristic of the experimental laser system showing the modal composition of the laser output as a function of the resonator round-trip length. The resonator length is given in units of the gain line center wavelength λ. For Gauss-Laguerre resonator modes TEM_{pls} (p angular, l radial, s longitudinal mode index) of transverse order $2p+l \leq 3$, the order and the longitudinal index of the family of degenerate modes contributing to the laser emission are indicated above the individual emission peaks.

aperture inserted into the resonator. Its diameter was chosen such that a further reduction of the diameter would have led to a significant increase of the laser threshold for the selected transverse-mode resonance of the cavity. In this way, large diffraction losses were introduced for all transverse modes except for the mode families of order $2p+l=1$, 2, or 3, so that only the resonant lowest-order transverse cavity modes were above laser threshold.

The Brewster windows of the Na_2 cell and the oblique reflection at the concave resonator mirror introduce astigmatic distortions of the intracavity field. In general such distortions destroy the cylindrical symmetry of the resonator, thereby leading to oscillation in Gauss-Hermite rather than Gauss-Laguerre modes.[43] In this case, generally beat oscillations or pulsations are observed in the laser output. They arise from the interference of nearly degenerate transverse modes, which are not phase locked, and oscillate at slightly different optical frequencies. Stationary emission with frequency-locked transverse modes can be expected only if the differences between the eigenfrequencies of the excited modes are significantly smaller than the resonator linewidth,[19,24] which in our system is $\kappa/2\pi \approx 3.5$ MHz. This regime of stationary laser operation was realized in our experiment in the following way.

For the optical resonator shown in Fig. 21, the astigmatic distortions of mirror and Brewster windows compensate each other to some extent. The residual astigmatism was compensated by a slightly asymmetric ray passage through the intracavity prism;[44] the required rotation of the Brewster prism in the plane of the resonator was $\leq 1°$. The criterion for a sufficient compensation of astigmatism was the absence of mode-beating oscillations in the laser output when the transverse-mode resonances of order $q=1$, 2, or 3 were excited. Outside the range of frequency locking, transverse-mode beat frequencies in the range of 0.5–5 MHz were observed.

Our theoretical analysis predicts that the shape and the stability of the field patterns forming in the considered laser system are strongly influenced by both the width of the transverse gain distribution and by the strength of pumping. The corresponding control parameters ψ and C introduced in Eqs. (2.3) and (2.10) denote the normalized Gaussian envelope radius and the normalized peak value of the small-signal gain coefficient of the transverse gain distribution, respectively. If one assumes a linear relation between optical pump intensity and small-signal laser gain, and that they have equal transverse profiles, the experimental value of the control parameter ψ is given by the ratio of the Gaussian envelope diameters of the pump field and of the intracavity laser field in the Na_2 cell. Correspondingly, the experimental value of the pump parameter C is proportional to the peak intensity in the center of the transverse section of the pump laser field. For a given value of ψ, the ratio between the actual pump power and the pump power for laser threshold, $P/P_{\rm thr}$ is therefore equal to the relative pump level $C/C_{\rm thr}$. In the experimental setup, the envelope radius of the intracavity field in the Na_2 cell was given by $w \approx 280$ μm according to the fixed resonator geometry. The pump beam diameter was set to various values covering the range $1<\psi<4$ by choosing suitable distances between the vapor cell and the lens collimating the pump beam. The intensity of the pump field was varied by changing the output power of the pump laser. Within the pump power range used in the experiments, the width and shape of the approximately Gaussian intensity profile of the pump laser showed no dependence on its output power.

B. Experimental observations

The stationary intensity patterns produced by the Na_2 laser were recorded photographically using a (24×36)-mm^2 camera whose lens was replaced by a beam expansion lens (focal length 20 mm) approximately 150 mm in front of the image plane. We note that the photographs shown here visualize the intensity distribution in the transverse section of the laser output without correctly reproducing the actual average output intensity, which may differ appreciably when the control parameters are changed. Figure 23 shows the output pattern of the laser for the case that the first-order transverse modes ($2p+l=1$) of the cavity are in resonance with the gain medium. The observed annular, cylindrically symmetric intensity distribution is in qualitative agreement with the predicted shape (see Fig. 2). This emission pattern is also known as the TEM_{01}^{*} hybrid mode.[45] The TEM_{01}^{*} pattern has a single phase singularity with a phase accumulation of $+2\pi$ or -2π around the symmetry center where the intensity is zero. Similar to earlier experiments with a

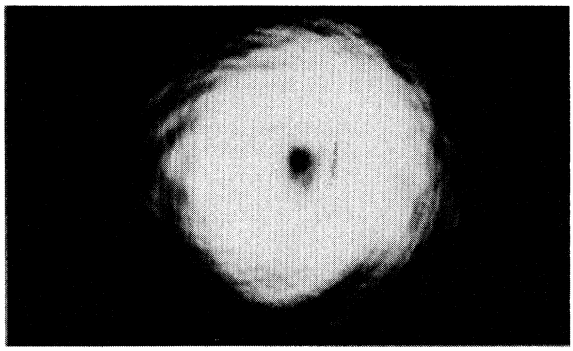

FIG. 23. Output intensity pattern of the laser for the case $2p+l=1$ (see text). The experimental parameters were $P/P_{\text{thr}}=3$, $\psi=2.1$, diameter of intracavity aperture 1.2 mm.

helium-neon laser,[37] the corresponding bistability of the optical phase pattern of the Na_2 laser could be demonstrated with the use of astigmatic imaging. In agreement with the predictions of Sec. III A, the TEM_{01}^{*} pattern was found to be stable in the whole pump intensity and pump beam collimation range that was studied (the corresponding range of the control parameter space is indicated in Fig. 25).

Figure 24 shows the four types of stationary patterns which were observed when the Gauss-Laguerre modes of order $2p+l=2$ were in resonance with the gain medium. The shapes of these patterns are in full qualitative agreement with the predicted shapes shown in Fig. 6 and correspond, respectively, to the cylindrically symmetrical, the 4H, the oval, and the doughnut configurations described in Sec. III B. It was found that the angular position of the patterns shown in Figs. 24(b) and 24(c), whose intensity distributions are not rotationally symmetric, was highly sensitive to the alignment of the pump beam and even to air turbulence. In fact, no preferred angular position exists for a pattern forming in a system of perfect cylindrical symmetry. Our experimental observations indicate that the angular position of patterns of broken cylindrical symmetry was in practice determined by the residual deviations from cylindrical symmetry in the experimental system.

For the case $2p+l=2$, the influence of intensity and collimation of the pump beam on the stability of the various emission patterns has been studied in the whole accessible control parameter range. The results are summarized in Fig. 25. The comparison with the calculated diagram shown in Fig. 5 indicates a large agreement with respect to the basic arrangement of the various domains of stability in parameter space. In particular, the predicted destabilization of the cylindrically symmetric patterns of the types shown in Figs. 24(a) and 24(d) for increasing pump levels also was observed experimentally. A more detailed study of the transition from emission in a Gauss-Laguerre TEM_{10} mode [Fig. 24(a)] to emission in a

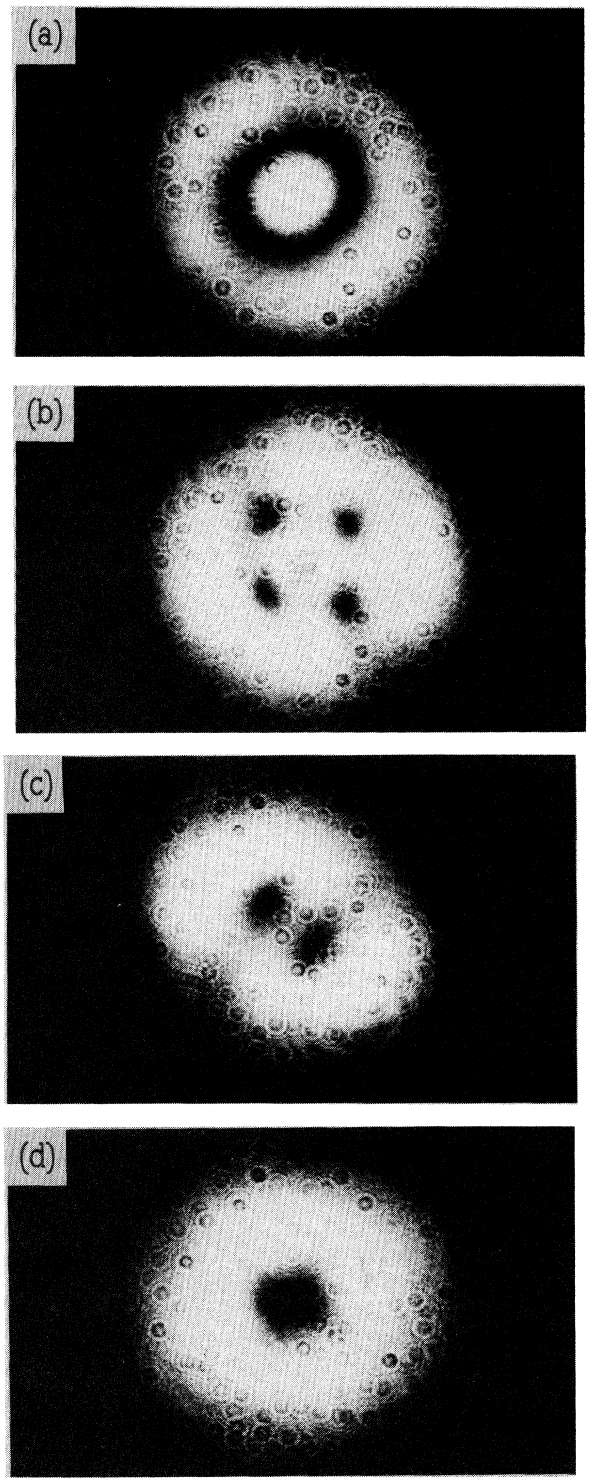

FIG. 24. Output intensity patterns observed for the case $2p+l=2$. (a) $P/P_{\text{thr}}=1.5$, $\psi=1.0$; (b) $P/P_{\text{thr}}=4.0$, $\psi=1.0$ (4H); (c) $P/P_{\text{thr}}=2.3$, $\psi=2.1$ (oval); (d) $P/P_{\text{thr}}=2.0$, $\psi=3.9$ (doughnut). In all cases the diameter of the intracavity aperture was 1.3 mm. The small-scale structures in the photographs are diffraction patterns caused by dust particles on a glass surface close to the camera. This complication was avoided for the other photographs shown here.

field pattern of broken symmetry [Fig. 24(b), 4H] has been carried out recently.[28]

Cases of bistability of the transverse field configuration were identified by the observation of hysteresis and switching when the pump beam was slightly displaced and then brought back to its original, approximately cylindrically symmetric position. Figure 25 shows the observed domain of bistability where the two intensity patterns shown in Figs. 24(b) (4H) and 24(c) (oval) were found to be both stable. For $\psi \approx 2.1$ and 2.4, switching between these two patterns could be induced by sweeping the pump intensity over the limits of the bistable range. With the same astigmatic imaging technique used also in the case of the TEM_{01}^{*} pattern (see above), bistability of the field pattern without change of the intensity pattern could be demonstrated for patterns of the type shown in Figs. 24(c) and 24(d).

For the effect of the control parameters on the stability of the field patterns formed by the transverse modes of order $2p+l=2$, we also observed significant discrepancies between theoretical and experimental results. In particular, a domain of bistablity where the 4H and the

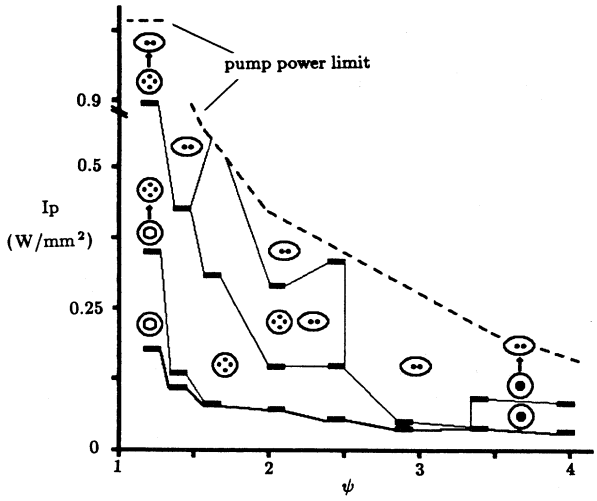

FIG. 25. Experimentally determined stability diagram for the case $2p+l=2$. The figure shows the stable emission patterns as a function of pump-beam collimation parameter ψ and pump-beam peak intensity I_p. The types of the stable patterns are represented by symbols relating to the patterns shown in Fig. 24. For a given value of ψ, the pump power was varied to identify the pump power levels where certain types of patterns became stable or unstable; the corresponding pump intensity values are indicated by horizontal bars. The thick line connecting the lowest-lying bars denotes the laser threshold. The other lines roughly indicate the arrangement of the various domains of stability as it can be inferred from the experimental observations. A domain where two different intensity patterns are stable lies in the approximate center of the diagram and for $\psi \approx 1.6$ extends to the pump power limit. The arrows denote the continuous changes of the shapes of the emission patterns which were observed when the pump intensity was varied. The diameter of the intracavity aperture was 1.3 mm.

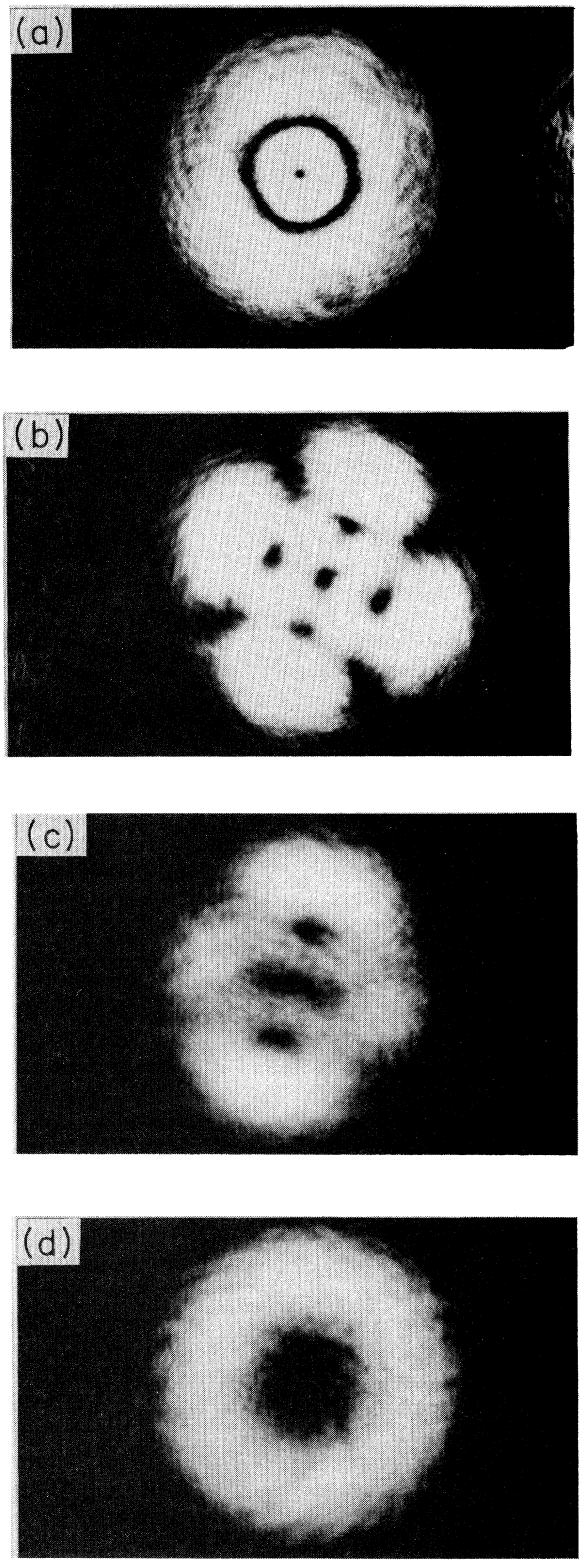

FIG. 26. Output intensity patterns observed for the case $2p+l=3$. (a) $P/P_{thr}=1.2$, $\psi=1.6$; (b) and (c) $P/P_{thr}=2.0$, $\psi=2.1$ (both patterns are stable for these parameters values); (d) $P/P_{thr}=1.6$, $\psi=3.9$. In all cases the diameter of the intracavity aperture was 1.6 mm.

doughnut patterns of Figs. 24(b) and 24(d) are both stable was not found, and the experimentally observed domain of bistability of the patterns of Figs. 24(b) and 24(c) is smaller than predicted. An unexpected phenomenon is also the continuous transition from the 4H pattern to the oval pattern for small ψ and increasing pump intensity (see Fig. 25). It may be noted that a common feature of these observations is the dominance of the oval pattern of Fig. 24(c) and the reduction in size of the stability domain of the 4H pattern of Fig. 24(b). Up to now, the origin of the discrepancies between predicted and observed stability characteristics is not clear. Our initial assumption that the deviations are related to the residual uncompensated astigmatism of the resonantor could not be verfied, as the same observations were made after various alignment procedures.

Figure 26 shows the four types of field patterns observed when the transverse modes of order $2p+l=3$ were resonantly excited. The characteristics of the patterns shown in Figs. 26(a)–26(d) agree with the numerically determined patterns shown in Figs 14(a), 14(d), 14(c), and 14(b), respectively. The photographs of Figs. 26 and 24 clearly demonstrate the structural relationship of the patterns forming for $2p+l=3$ and 2: even if the modal composition of both sets of patterns is dissimilar, the only characteristic difference is the additional phase singularity in the center of each of the patterns of the $2p+l=3$ configuration. The location of the domains of stability of related patterns in the experimental control parameter space was found to be very similar. In particular, one also observes a domain of bistability where the patterns of Figs. 26(b) and 26(c) are both stable. Patterns with seven and nine phase singularities of the type shown in Figs. 14(e) and 14(f) were observed at some occasions for control parameters close to the stability domain of the five-singularity pattern of Fig. 26(b). The observations of these patterns were not completely reproducible, probably because the experimental stability domain of these patterns is very small.

A characteristic modification of the shape of the emitted patterns was observed for the case where the diameter of the intracavity aperture of the laser was increased beyond the values indicated in Figs. 23–26 so that higher-order frequency-degenerate transverse modes could contribute to the laser emission (see Sec. V A). In all cases except the one noted in the following, the bright peripheral regions of the patterns simply increased in size without further changes of the basic structure of the pattern. One example for this effect is shown in Fig. 27(a), which should be compared to Fig. 26(a). A particular phenomenon was observed under conditions where the laser emitted a pattern of the type shown in Fig. 26(b). Upon increasing the aperture diameter, here four additional phase singularities are formed and integrated into the regular arrangement of the other phase singularities [see Fig. 27(b)].

VI. CONCLUDING REMARKS

In Sec. IV we have demonstrated in detail the analogy between the phase singularities that are formed in the interaction of the transverse modes belonging to a frequency-degenerate family and the defects[46] called vortices in such fields as, for example, hydrodynamics, superconductivity, and superfluidity. A point which remains to be elucidated is the relation between these phase singularities and the optical vortices discovered by Coullet and collaborators.[33] In the steady state, the optical vortices occupy positions that depend on the initial conditions, whereas the phase singularities discussed in this paper are arranged in the form of regular crystals. Our phase singularities arise from the interaction of few modes, whereas the vortices of Ref. 33 are the result of the interplay of a very large number of modes. However, it is not at all obvious that phase singularities are intrinsically different from optical vortices. As a matter of fact, on the local scale around the zero-field points, the vortices of Ref. 33 have the same structure as the singularities in this paper. Coullet and collaborators consider an essentially isolated optical vortex which exhibits a large-scale spiral structure for the equiphase lines; however, if several vortices and antivortices are brought together, the spiral structure can disappear, and the configuration can be much more similar to those we find in our analysis. In order to clarify the relation with the optical vortices, it is

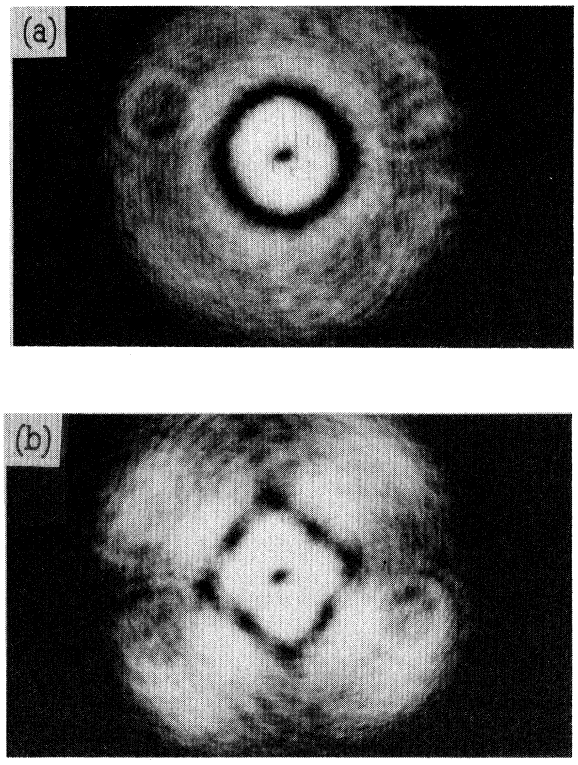

FIG. 27. Output intensity patterns for the case $2p+l=3$. Here the diameter of the intracavity aperture is sufficiently large (2 mm) to have no longer any effect on the size of the emitted patterns (see text). All other experimental conditions for the mode patterns (a) and (b) are identical to those of Figs. 26(a) and 26(b), respectively.

presumably necessary to extend the analysis beyond the case of a frequency-degenerate family and beyond the situations in which the system approaches a stationary state. Particularly interesting is the theoretical and experimental investigation of cases in which the system develops turbulent dynamics, showing complex spatiotemporal behavior of the optical vortices or phase singularities, possibly giving rise to a "defect-mediated turbulence," as predicted by Coullet and collaborators.[47]

The comparison between the theoretical predictions and the experimental data for the case $2p+l=2$ exhibits a satisfactory amount of qualitative agreements. There are, however, also some discrepancies, which arise mainly from the fact that the domain of existence of the 4H configuration in the (C,ψ) plane of the control parameter is much more restricted in the experimental picture. A possible explanation for this fact is that in our calculations we do not include an element which is present in the experiment, namely, the aperture. Or, more precisely, we consider only the limit of infinite aperture. We are now extending our calculations by considering the aperture in the form of a radially dependent loss parameter, as described in Ref. 36. Preliminary results for the case $2p+l=2$ show that the theoretical predictions move in the direction of increased agreement with the experimental results, in the sense that the domain of existence of the 4H configuration in the (C,ψ) plane is reduced, and there is no region in which the 4H and the doughnut patterns coexist.

Note added in proof

The possibility of generating defects in the electromagnetic field was first predicted, and extensively analyzed, in an outstanding series of papers by Berry, Nye, and collaborators [see, for example, J. F. Nye and M. V. Berry, Proc. R. Soc. London, Ser. A **336**, 165 (1974); M. V. Berry, J. F. Nye, and F. J. Wright, Philos. Trans. R. Soc. London Ser. A **291**, 453 (1979); F. J. Nye, Proc. R. Soc. London Ser. A **387**, 105 (1983); Refs. 32, 38, 41, 54, 59, and 65 in the list of references in Ref. 46], which is reviewed in Ref. 46 of this paper. These authors considered the linear, scalar wave equation and identified several appropriate solutions that display a wide variety of defects such as, for example, dislocations. These patterns can exhibit rich and complex structures, sometimes on different spatial scales simultaneously, including the subwavelength scale. Especially interesting is the elliptic umbilic diffraction catastrophe, which displays a crystal-like fine structure of dislocation lines predicted and experimentally observed by the same authors.

With reference to the classification of defects given in Ref. 46, from a three-dimensional viewpoint our phase singularities correspond to screw dislocations. This fact is immediately seen if we consider the complete phase of the electric field which, according to Eqs. (2.4) and (2.19), is given by

$$\phi-\bar{\omega}_q+k_q z \ ,$$

where ϕ is the phase of the envelope F. Clearly, if we move along the longitudinal axis z the equiphase lines in the transverse planes generate equiphase surfaces which, in a transverse neighborhood of the singularity, have a helix shape. Our patterns display a transverse spatial variation that develops on a scale much larger than a wavelength. They arise spontaneously from the mode-mode competition induced by the interaction of the radiation field with the nonlinear medium. The nonlinearity of the dynamics is in this case the essential element which governs the phenomenology, via a well-defined set of instabilities. The controlled variation of the parameters activates the various instabilities and primes the transition from the nonlasing state to laser emission, or the transition from one pattern to another.

ACKNOWLEDGMENTS

We thank N. B. Abraham for some stimulating discussions at an early stage of this work. This research was carried out in the framework of the ESPRIT Basic Research Action on "Transverse Optical Patterns."

*Also at Physik-Institut, Universität Zürich, Zürich, Switzerland.

[1]J. Opt. Soc. Am. B **2** (1) (1985), special issue on instabilities in active optical media.

[2]J. Opt. Soc. Am. B **5** (1) (1988), special issue on nonlinear dynamics of lasers.

[3]*Instabilities and Chaos in Quantum Optics,* edited by F. T. Arecchi and R. Harrison (Springer-Verlag, Berlin, 1987).

[4]N. B. Araham, P. Mandel, and L. M. Narducci, in *Progress in Optics,* edited by E. Wolf (North-Holland, Amsterdam, 1988), Vol. XXV, p. 1; *Instabilities and Chaos in Quantum Optics II,* edited by N. B. Abraham, F. T. Arecchi, and L. A. Lugiato (Plenum, New York, 1988).

[5]C. O. Weiss and J. Brock, Phys. Rev. Lett. **57**, 2804 (1986).

[6]A. M. Turing, Philos. Trans. R. Soc. London Ser. B **237**, 37 (1952).

[7]H. Haken, *Synergetics: An Introduction* (Springer-Verlag, Berlin, 1977).

[8]G. Nicolis and I. Prigogine, *Self-Organization in Nonequilibrium Systems* (Wiley, New York, 1977).

[9]A. F. Suchkov, Zh. Eksp. Teor. Fiz. **49**, 1495 (1965) [Sov. Phys.—JETP **22**, 1026 (1966)]; R. G. Allakhverdyan, A. N. Oraevsky, and A. F. Suchkov, Fiz. Tekh. Poluprovdn. **4**, 341 (1970) [Sov. Phys.—Semicond. **4**, 227 (1970)].

[10]V. E. Kuzin and A. F. Suchkov, Kvant. Elektron. (Moscow) **2**, 53 (1972) [Sov. J. Quantum Electron. **2**, 236 (1972)]; I. M. Belousova, G. N. Vinokurov, O. B. Danilov, and N. N. Rozanov, Zh. Eksp. Teor. Fiz. **52**, 1146 (1967) [Sov. Phys.—JETP **25**, 761 (1967)].

[11]P. W. Smith, Appl. Phys. Lett. **13**, 235 (1968); D. H. Austen, IEEE J. Quantum Electron. **QE-5**, 471 (1968).

[12]J. H. Moloney, in *Instabilities and Chaos in Quantum Optics* (Ref. 3), p. 139ff; *Progress in Optics* (Ref. 4), p. 193ff, and references quoted therein; N. N. Rozanov, V. E. Semenov, and G. V. Khodorova, Kvant. Elektron. (Moscow) **9**, 356 (1982) [Sov. J. Quantum Electron. **12**, 193 (1982)].

[13]W. J. Firth, in *Progress in Optics* (Ref. 4), p. 219ff and references quoted therein; M. Le Berre, E. Ressayre, and A. Tal-

let, Phys. Rev. A **25**, 1604 (1982).
[14]L. A. Lugiato and R. Lefever, Phys. Rev. Lett. **50**, 220 (1987).
[15]S. Akhmanov, in *Quantum Optics VI,* edited by J. H. Eberly, L. Mandel, and E. Wolf (Plenum, New York, 1990).
[16]G. Grynberg, E. Le Bihan, P. Verkerk, P. Simoneau, J. R. R. Leite, D. Bloch, S. Le Boiteux, and M. Duclay, Opt. Commun. **67**, 363 (1988); G. Giusfredi, J. F. Valley, R. Pon, G. Khitrova, and H. M. Gibbs, J. Opt. Soc. Am B **5**, 1181 (1988).
[17]P. Hollinger and C. Jung, J. Opt. Soc. Am. B **2**, 218 (1985).
[18]A. L. Gaeta, M. K. Skeldon, R. W. Boyd, and P. Narum, IEEE J. Quantum Electron. **QE-22**, 2161 (1986).
[19]L. A. Lugiato, C. Oldano, and L. M. Narducci, J. Opt. Soc. Am. B **5**, 879 (1988).
[20]H. G. Winful and S. S. Wang, Appl. Phys. Lett. **53**, 1894 (1988).
[21]L. A. Lugiato, G. L. Oppo, M. A. Pernigo, J. R. Tredicce, L. M. Narducci, and D. K. Bandy, Opt. Commun. **68**, 63 (1988).
[22]L. A. Lugiato, F. Prati, L. M. Narducci, P. Ru, J. R. Tredicce, and D. K. Bandy, Phys. Rev. A **37**, 3847 (1988).
[23]L. A. Lugiato, F. Prati, L. M. Narducci, and G. L. Oppo, Opt. Commun. **69**, 387 (1989).
[24]L. A. Lugiato, G. L. Oppo, J. R. Tredicce, and L. M. Narducci, J. Opt. Soc. Am. B **7**, 1019 (1990).
[25]J. Opt. Soc. Am. B **7**(6) (1990); **7**(7) (1990); special issues on transverse effects in nonlinear optical systems.
[26]J. R. Tredicce, E. J. Quel, A. M. Ghazzawi, C. Green, M. A. Pernigo, L. M. Narducci, and L. A. Lugiato, Phys. Rev. Lett. **62**, 1274 (1989).
[27]C. Tamm, Phys. Rev. A **38**, 5960 (1988).
[28]C. Tamm and C. O. Weiss, Opt. Commun. (to be published).
[29]J. M. Kosterlitz and D. J. Thouless, J. Phys. C **6**, 1181 (1973).
[30]N. M. Mermin, Rev. Mod. Phys. **51**, 591 (1979).
[31]P. Minnhagen, Rev. Mod. Phys. **59**, 1001 (1987); P. D. McCormack and L. Crane, *Physical Fluid Dynamics* (Academic, New York, 1973).
[32]H. Lamb, *Hydrodynamics* (Cambridge University, Cambridge, 1932).
[33]P. Coullet, L. Gil, and F. Rocca, Opt. Commun. **73**, 403 (1989).
[34]F. Diedrich, E. Peik, J. M. Chen, W. Quint, and H. Walther, Phys. Rev. Lett. **59**, 2931 (1987).
[35]H. Kogelnik, in *Lasers: A Series of Advances,* edited by A. K. Levine (Dekker, New York, 1966), Vol. 1, p. 295.
[36]It is straightforward to generalize Eq. (2.8) to include diffraction losses. In fact, one must simply replace the term $-kf_{\rm pli}$ by $-k\int_0^{2\pi}d\varphi\int_0^{\infty}d\rho\,\rho A_{\rm pli}(\rho,\varphi)\xi(\rho)F(\rho,\varphi,t)$, where the function $\xi(\rho)$ describes the radial distribution of the losses. For $\xi(\rho)\neq$const, this term has the effect that each mode has a different loss parameter.
[37]C. Tamm, J. Opt. Soc. Am. B (to be published).
[38]P. M. Morse and M. Feshbach, *Methods of Theoretical Physics* (McGraw-Hill, New York, 1983), Vol. I.
[39]D. R. Tilley and J. Tilley, *Superfluidity and Superconductivity* (Hilger, Bristol, 1986).
[40]M. Brambilla, L. A. Lugiato, V. Penna, F. Prati, C. Tamm, and C. O. Weiss, following paper, Phys. Rev. A **43**, 5114 (1991).
[41]B. Wellegehausen, IEEE J. Quantum Electron. **QE-15**, 1108 (1979).
[42]H. Kogelnik and T. Li, Appl. Opt. **5**, 1550 (1966).
[43]D. C. Hanna, IEEE J. Quantum Electron. **QE-5**, 483 (1969).
[44]See, e.g., A. E. Siegman, *Lasers* (University Science, Mill Valley, CA, 1986), p. 647–648.
[45]W. W. Rigrod, Appl. Phys. Lett. **2**, 51 (1963).
[46]M. Berry, in *Physics of Defects,* Les Houches Session XXXV, edited by R. Balian *et al.* (North-Holland, Amsterdam, 1980).
[47]P. Coullet, L. Gil, and S. Lega, Phys. Rev. Lett. **62**, 1619 (1989); Physica D **37**, 91 (1989).

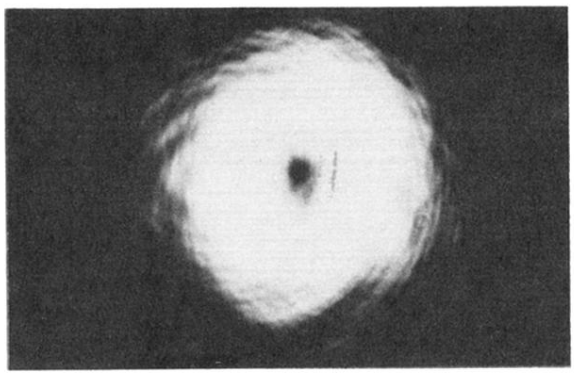

FIG. 23. Output intensity pattern of the laser for the case $2p+l=1$ (see text). The experimental parameters were $P/P_{\text{thr}}=3$, $\psi=2.1$, diameter of intracavity aperture 1.2 mm.

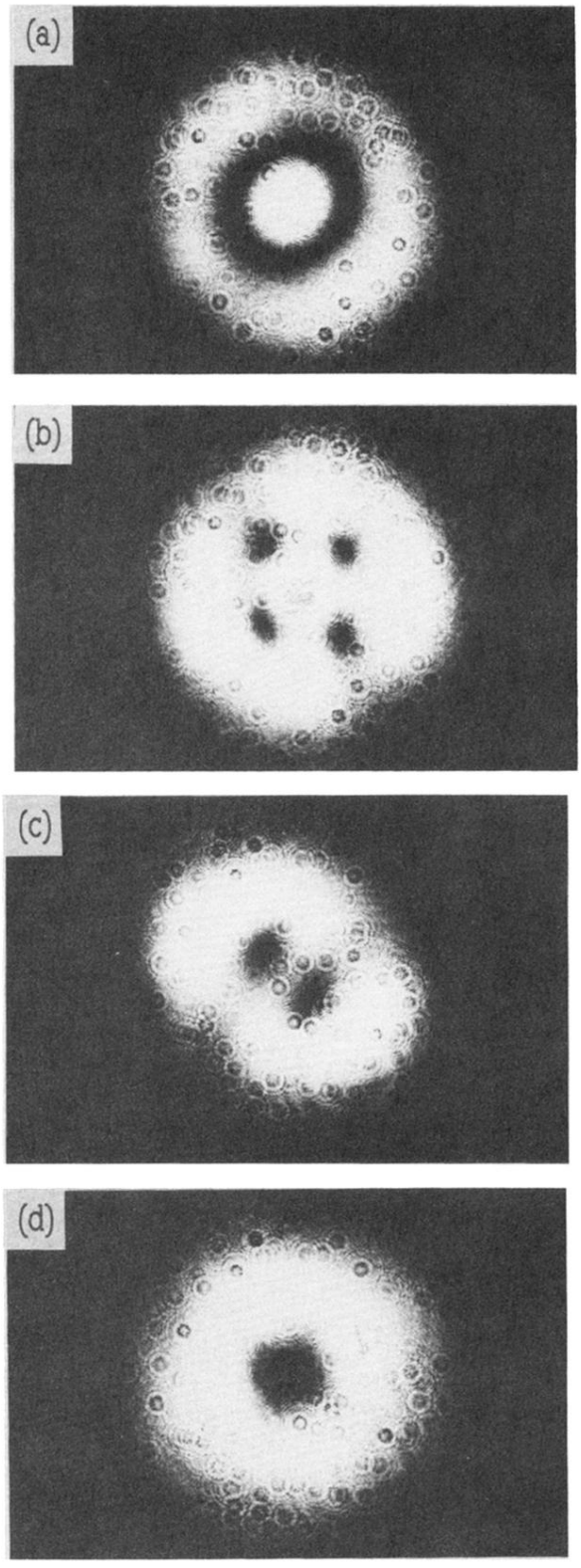

FIG. 24. Output intensity patterns observed for the case $2p+l=2$. (a) $P/P_{thr}=1.5$, $\psi=1.0$; (b) $P/P_{thr}=4.0$, $\psi=1.0$ (4H); (c) $P/P_{thr}=2.3$, $\psi=2.1$ (oval); (d) $P/P_{thr}=2.0$, $\psi=3.9$ (doughnut). In all cases the diameter of the intracavity aperture was 1.3 mm. The small-scale structures in the photographs are diffraction patterns caused by dust particles on a glass surface close to the camera. This complication was avoided for the other photographs shown here.

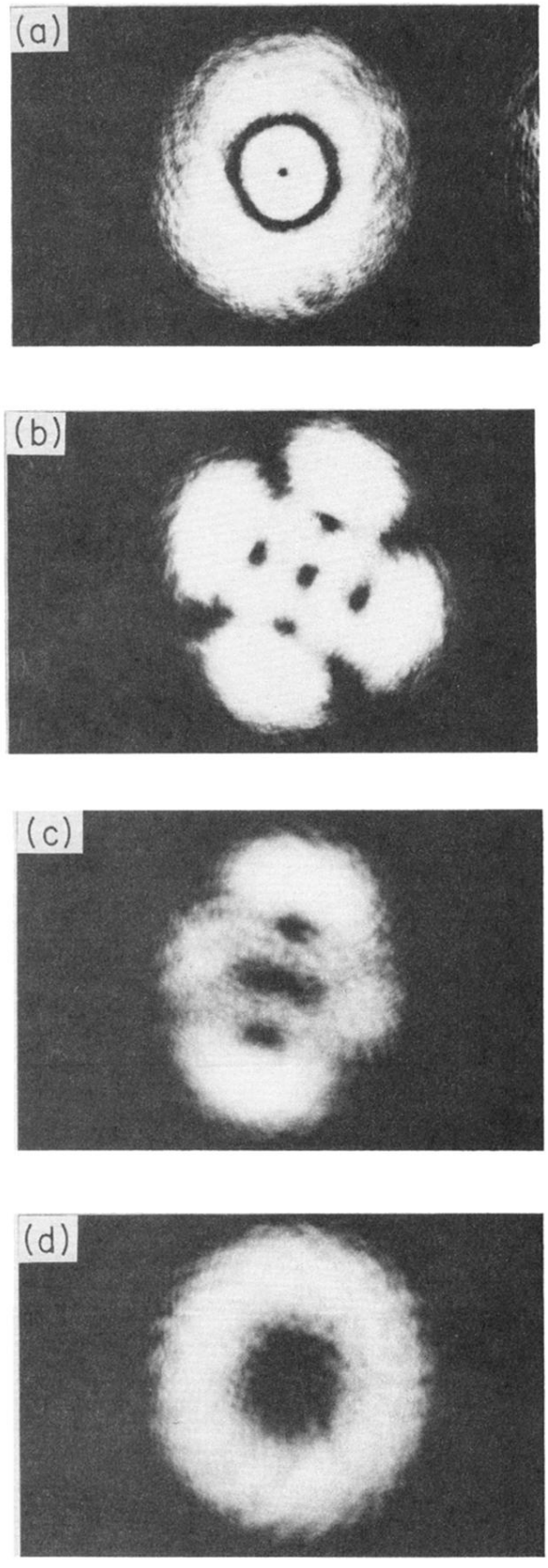

FIG. 26. Output intensity patterns observed for the case $2p+l=3$. (a) $P/P_{thr}=1.2$, $\psi=1.6$; (b) and (c) $P/P_{thr}=2.0$, $\psi=2.1$ (both patterns are stable for these parameters values); (d) $P/P_{thr}=1.6$, $\psi=3.9$. In all cases the diameter of the intracavity aperture was 1.6 mm.

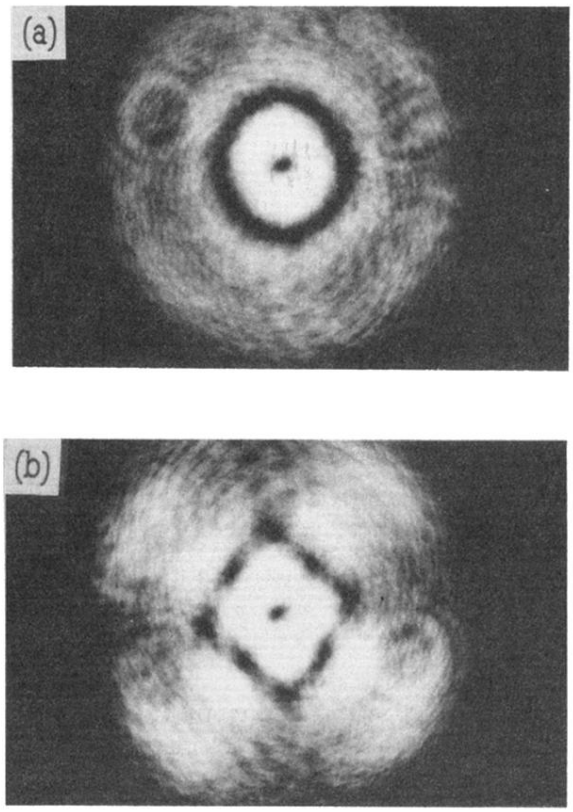

FIG. 27. Output intensity patterns for the case $2p + l = 3$. Here the diameter of the intracavity aperture is sufficiently large (2 mm) to have no longer any effect on the size of the emitted patterns (see text). All other experimental conditions for the mode patterns (a) and (b) are identical to those of Figs. 26(a) and 26(b), respectively.